Check for updates

JGR Planets

RESEARCH ARTICLE

10.1029/2025JE009490

Modeling Wind-Driven Waves on Other Planets: Applications to Mars, Titan, and Exoplanets

Una G. Schneck[1], Charlene E. Detelich[2], Milan Curcic[3,4], Andrew D. Ashton[5], Alexander G. Hayes[2], and J. Taylor Perron[1]

[1]Department of Earth, Atmospheric, and Planetary Sciences, Massachusetts Institute of Technology, Cambridge, MA, USA, [2]Department of Astronomy, Cornell University, Ithaca, NY, USA, [3]Department of Ocean Sciences, Rosenstiel School of Marine, Atmospheric and Earth Science, University of Miami, Miami, FL, USA, [4]Frost Institute for Data Science and Computing, University of Miami, Coral Gables, FL, USA, [5]Woods Hole Oceanographic Institution, Woods Hole, MA, USA

Abstract Waves could exist on any planet with sustained winds and stable surface liquids. However, differences in atmospheres, liquids, and gravity confound efforts to extend Earth-based empirical wave models to other planetary environments. We adapted a physics-based numerical wave model to study how planetary conditions affect the growth of waves. We modeled lakes of water on ancient Mars, liquid nitrogen and hydrocarbons on past and present Titan, sulfuric acid on the exo-Venus Kepler 1649-b, liquid water on the super-Earth LHS 1140-b, and liquid rock on the super-Earth 55 Cancri-e. We find that the threshold for wave generation is lower for liquids with weaker surface tension and under higher atmospheric pressure and lower gravity. We also find that waves grow taller in less dense liquids and under higher atmospheric pressure and lower gravity. This suggests that waves on Titan and ancient Mars will begin to grow under weaker winds and grow taller than the equivalent waves on Earth, with a decrease in wave height and an increase in the wave generation threshold as the atmospheric pressure is reduced. Kepler 1649-b and LHS 1140-b both have higher threshold wind speeds and shorter waves. The liquid rock of 55 Cancri-e leads to an even larger wind speed threshold with smaller waves. Our work suggests that the occurrence and size of waves strongly depend on planetary conditions, which affect the timescale and magnitude of shoreline modification, sediment transport, and fluid mixing–ultimately impacting a planet's climate and long-term landscape evolution.

Plain Language Summary Wind blowing over water creates waves that move sediment and shape Earth's shorelines. This process should vary on other planets with different liquids, atmospheres, and gravity. However, modern wave models calibrated to Earth are not applicable. We developed a wave model that is flexible enough to apply to any planet and apply it to Mars, Titan, and three exoplanets that could have lakes or oceans of sulfuric acid (Kepler 1649-b), water (LHS 1140-b), and liquid rock (55 Cancri-e). We find that the threshold wind speed to create waves decreases as surface tension decreases, atmospheric pressure increases, or gravity decreases. The wave height increases as liquid density decreases, atmospheric pressure increases, or gravity decreases. Waves on Mars and Titan begin to grow for weak winds and grow taller compared to Earth. Waves on the exo-Venus Kepler 1649-b, the super-Earth LHS 1140-b, and the super-Earth 55 Cancri-e start to grow for stronger winds and are smaller than the equivalent waves on Earth. This shows that planetary conditions are important to consider when studying waves beyond Earth and their potential to modify the climate and surface.

Key Points:

- A model for wind-driven waves, flexible to planetary conditions, is applied to past Mars, past and present Titan, and three exoplanets
- Wind-driven waves in crater lakes could have occurred in Mars' past with a size that depended on crater shape
- Wind-driven waves of liquid hydrocarbons on Titan are taller, slower, and have a lower wind speed threshold (>~0.5 m/s) than Earth

Supporting Information:

Supporting Information may be found in the online version of this article.

Correspondence to:

U. G. Schneck,
uschneck@mit.edu

Citation:

Schneck, U. G., Detelich, C. E., Curcic, M., Ashton, A. D., Hayes, A. G., & Perron, J. T. (2026). Modeling wind-driven waves on other planets: Applications to Mars, Titan, and exoplanets. *Journal of Geophysical Research: Planets*, *131*, e2025JE009490. https://doi.org/10.1029/2025JE009490

Received 14 OCT 2025
Accepted 4 MAR 2026

Author Contributions:

Conceptualization: Una G. Schneck, Charlene E. Detelich, Milan Curcic, Alexander G. Hayes
Data curation: Una G. Schneck
Formal analysis: Una G. Schneck, Charlene E. Detelich, Milan Curcic
Funding acquisition: Andrew D. Ashton, Alexander G. Hayes, J. Taylor Perron
Investigation: Una G. Schneck, Charlene E. Detelich, Milan Curcic
Methodology: Una G. Schneck, Charlene E. Detelich, Milan Curcic, Andrew D. Ashton, Alexander G. Hayes, J. Taylor Perron
Resources: Una G. Schneck, Milan Curcic, Alexander G. Hayes, J. Taylor Perron

© 2026. The Author(s).
This is an open access article under the terms of the Creative Commons Attribution License, which permits use, distribution and reproduction in any medium, provided the original work is properly cited.

1. Introduction

Wind-driven surface waves drive measurable change on Earth's coastlines through processes of erosion and sediment redistribution. However, Earth is only one among a growing population of planets and moons with known lakes and oceans on their past or present-day surfaces. Wave action could therefore be a widespread surface process on planets with sustained atmospheres and liquids on their surface. Waves can also be an important means by which the atmosphere shapes the landscape (e.g., Ashton et al., 2009; Huppert et al., 2020; Komar, 1998; Nienhuis et al., 2015, and many others). The atmosphere is, in turn, affected by wind waves that impose a variable surface roughness and temperature gradient on the wind, which can control the size and character of the atmospheric boundary layer (Janssen, 1989) and affect the overall climate (Khuller & Clow, 2024). The existence of waves also distorts the surface of the liquid, which could allow for remote detection

21699100, 2026, 4, Downloaded from https://agupubs.onlinelibrary.wiley.com/doi/10.1029/2025JE009490 by Cochrane Russian Federation, Wiley Online Library on [30/04/2026]. See the Terms and Conditions (https://onlinelibrary.wiley.com/terms-and-conditions) on Wiley Online Library for rules of use; OA articles are governed by the applicable Creative Commons License

Software: Una G. Schneck, Charlene E. Detelich, Milan Curcic, Alexander G. Hayes
Supervision: Milan Curcic, Andrew D. Ashton, Alexander G. Hayes, J. Taylor Perron
Validation: Una G. Schneck, Charlene E. Detelich, Milan Curcic
Visualization: Una G. Schneck, Alexander G. Hayes
Writing – original draft: Una G. Schneck
Writing – review & editing: Charlene E. Detelich, Milan Curcic, Andrew D. Ashton, Alexander G. Hayes, J. Taylor Perron

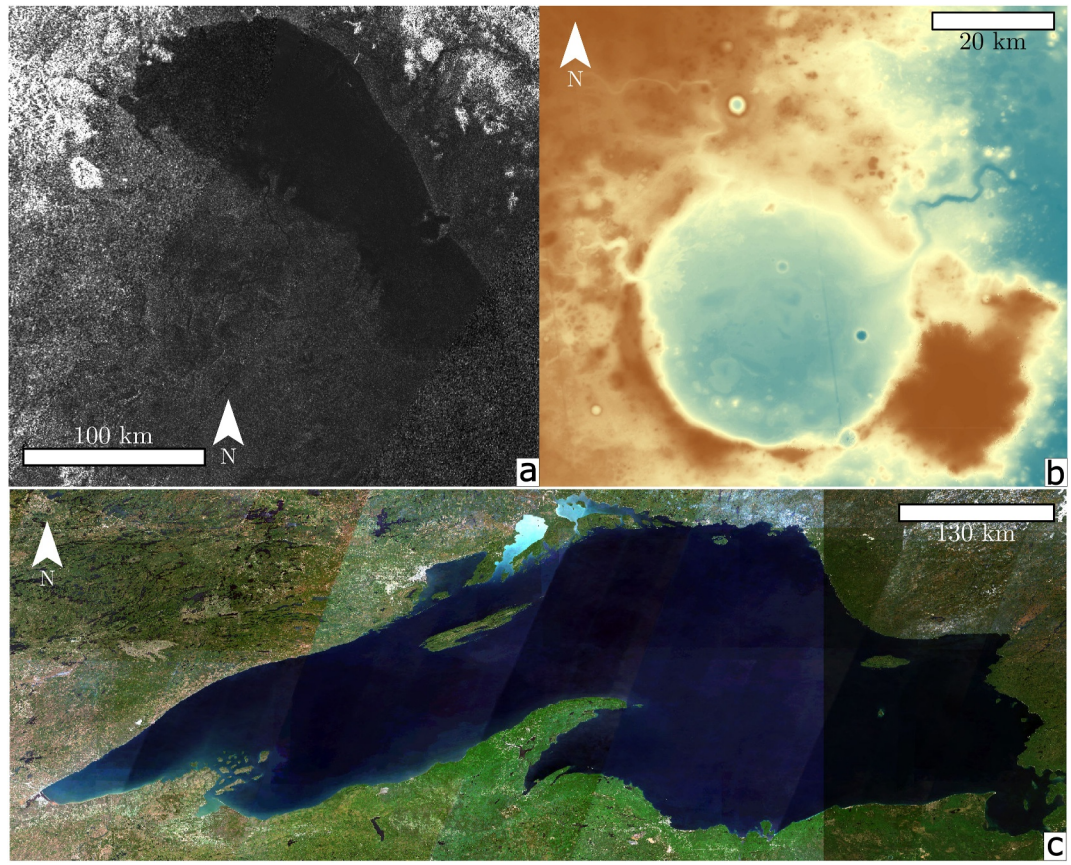

Figure 1. Lakes in the solar system, past and present. (a) Ontario Lacus, Titan. Liquid hydrocarbon lake as viewed by the Cassini K_u-band synthetic aperture radar. (b) Jezero crater, putatively a former crater lake of liquid water, Mars. Context Camera (CTX) and High-Resolution Imaging Science Experiment (HiRISE) digital terrain model (DTM) mosaic. (c) Lake Superior, Earth. Mosaic (2017–2020) of cloud-free images in RGB bands of Sentinel-2.

of lakes and oceans (Barnes et al., 2011; Donelan & Pierson, 1987; Zugger et al., 2010). In addition, waves are also a means of efficient transport and mixing within lakes and oceans, which has important implications for chemistry and biology (Imboden & Wüest, 1995).

Within our solar system, past Mars and present Titan show evidence of extensive liquid on their surfaces (Figure 1; Stofan et al., 2007; Wordsworth, 2016). Beyond our own solar system, a variety of exoplanets may lie within the stability range of water or more exotic liquids (Figure 2; Seager, 2013). The Kepler space telescope and the James Webb Space Telescope (JWST) have ushered in a new era of exoplanet characterization, including rocky super-Earths and exo-Venuses with large atmospheres sustained by putative liquid water, sulfuric acid, and liquid rock oceans across their surface (Angelo et al., 2017; Cadieux, Doyon, et al., 2024; Cadieux, Plotnykov, et al., 2024; Hu et al., 2024).

Presently, the atmospheric pressure and surface temperature of Mars are generally too low to allow liquid water to be stable (Figure 2); however, there is substantial evidence for past liquid water on Mars' surface (Mangold et al., 2021; Wordsworth, 2016). The details of Mars' surface hydrologic record remain hotly debated (Wordsworth, 2016), but current geomorphologic and mineralogical evidence suggests a semi-arid model of Martian climate into the Amazonian period (<~3.0 Gya) which was punctuated by intense periods of wetting that formed valley networks and crater lakes and reoccurred and/or survived regularly enough to form deltaic deposits over the globe (De Toffoli et al., 2021; Di Achille & Hynek, 2010; Dickson et al., 2021; Ehlmann et al., 2011; Kite et al., 2015; Mangold et al., 2021; Schon et al., 2012). Further sedimentological analysis of lake deposits at Gale crater suggests that some of these lakes may have been liquid and ice-free long enough to form ripples in the bed that may have been preserved in rocks (Mondro et al., 2025; Rubin et al., 2022).

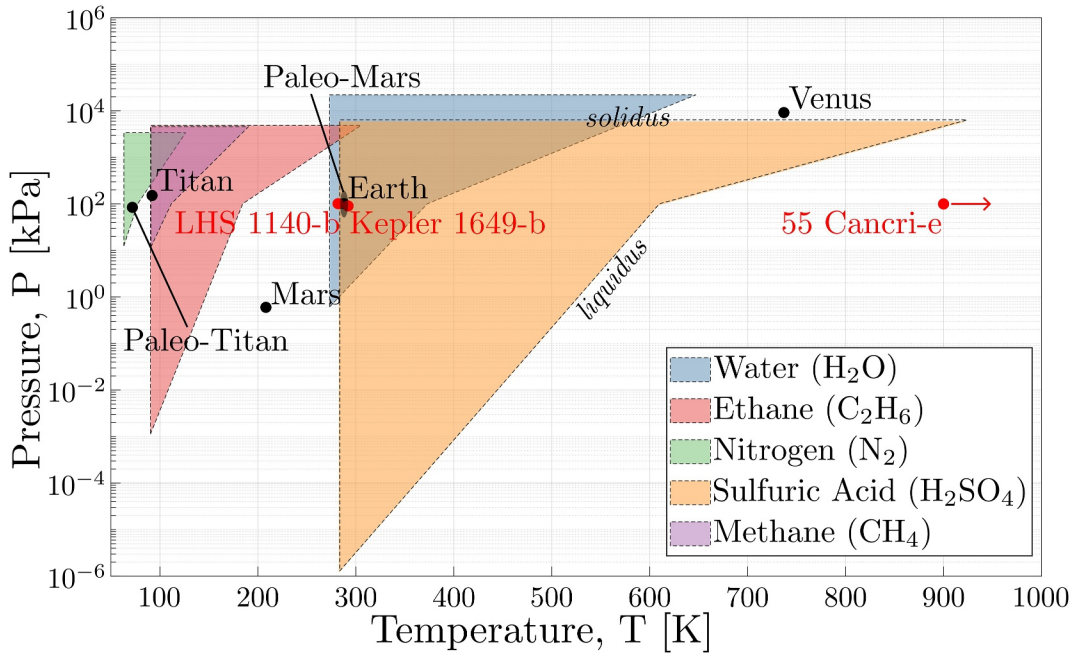

Figure 2. Pressure-Temperature regimes for liquid stability compared with past and current planetary surfaces. For each material, the liquidus line is approximated based on the triple point, normal boiling point (boiling point at 1 atm of pressure), and critical point, and the solidus line is approximated based on the triple point, normal melting point (melting point at 1 atm of pressure), and critical point (Thomson, 1996). Black circles represent typical temperature-pressure regimes for planets within our solar system (Table 1). Red circles indicate possible temperature-pressure regimes for exoplanets explored in this paper (Table 1). The red arrow for 55 Cancri-e represents surface conditions that exceed the axis limits (~100 kPa, ~1,500 K).

In contrast, Saturn's moon Titan is the only other body in the solar system that presently supports stable liquids on its surface as part of an active hydrologic cycle. The lakes on the surface of Titan are made of a mixture of hydrocarbons, primarily methane and ethane, and dissolved nitrogen (Brown et al., 2008; Cordier et al., 2009; Hayes, 2016; Malaska & Hodyss, 2014; Mastrogiuseppe et al., 2019; Stofan et al., 2007; Zebker et al., 2014), with the exact composition appearing to vary with latitude and season (Hayes, 2016; Le Gall et al., 2016; Mastrogiuseppe et al., 2018; Poggiali et al., 2020, 2024). Past work (Palermo et al., 2024; Wall et al., 2010) has suggested that the shorelines of these lakes may have been modified by wave action, but the direct observation of waves has proved difficult (Barnes et al., 2011; Grima et al., 2017; Hayes et al., 2013; Wye et al., 2009). Later in the *Cassini* mission, surface roughening was observed on isolated patches of some lakes but could not be definitively ascribed to waves (Barnes et al., 2014; Heslar & Barnes, 2025; Heslar et al., 2020; Poggiali et al., 2024). Despite previous studies suggesting that waves should form easily under Titan conditions (Ghafoor et al., 2000; Lorenz et al., 2005, 2010; Lorenz & Hayes, 2012), their existence and extent remains contested.

By comparison, the surfaces of exoplanets may be extreme environments unlike anything that exists on Earth (Seager & Dotson, 2010). Of these, some worlds could host isolated or global oceans of exotic stable liquids (e.g., sulfuric acid, liquid nitrogen, liquid rock; Figure 2). Attempts to directly observe these liquids is ongoing, but the frequency and size of large waves could affect the measured light curve (Zugger et al., 2010). Like Earth, these waves could also impact atmospheric circulation and shorelines.

Previous wave models have provided foundational insight into the behavior of waves beyond Earth (Ghafoor et al., 2000; Hayes et al., 2013; Lorenz et al., 2005, 2010; Lorenz & Hayes, 2012), but they often rely on terrestrial empiricisms, Earth-like conditions, or simplified mechanisms of generation and dissipation that limits our ability to predict the effect of waves in a larger planetary context. This may explain the discrepancy between predicted wave growth and the observed surface smoothness of Titan's lakes (<10 mm roughness (Grima et al., 2017; Poggiali et al., 2024; Wye et al., 2009; Zebker et al., 2014)). In addition, no wave modeling for extreme environments like those present on exoplanets has ever been attempted. In this paper, we present a physics-based wave model, expanded from Hayes (2013), that can be applied to any planetary conditions. We explore how differences

21699100, 2026, 4, Downloaded from https://agupubs.onlinelibrary.wiley.com/doi/10.1029/2025JE009490 by Cochrane Russian Federation, Wiley Online Library on [30/04/2026]. See the Terms and Conditions (https://onlinelibrary.wiley.com/terms-and-conditions) on Wiley Online Library for rules of use; OA articles are governed by the applicable Creative Commons License

21699100, 2026, 4, Downloaded from https://agupubs.onlinelibrary.wiley.com/doi/10.1029/2025JE009490 by Cochrane Russian Federation, Wiley Online Library on [30/04/2026]. See the Terms and Conditions (https://onlinelibrary.wiley.com/terms-and-conditions) on Wiley Online Library for rules of use; OA articles are governed by the applicable Creative Commons License

in the atmosphere, liquid, and gravity affect the growth of waves in the lakes and oceans of Titan, paleo-Mars, and three possible exoplanets, including the exo-Venus Kepler 1649-b with sulfuric acid lakes, the super-Earth LHS 1140-b with liquid water lakes, and the super-Earth 55 Cancri-e with molten lava lakes.

2. Wave Model

On Earth, waves form as wind blows over water and exchanges energy with the liquid through shear and pressure fluctuations. The maximum size of the waves depends primarily on the strength and duration of the wind and the distance over which it blows ("fetch"). As the waves grow longer, their restoring force shifts from predominantly surface tension ("capillary waves") to gravity ("gravity waves"). For any given wind climate, many frequencies of waves are excited within the liquid and will grow and interact as they evolve toward an equilibrium state. When the wave spectrum becomes stationary (i.e., at equilibrium), we consider the waves to be fully developed.

The spectral wave model developed for this paper (*PlanetWaves*) produces a four-dimensional spectrum of liquid surface elevations $F(x, y, \omega, \theta)$ in response to an applied wind climate, where η is the deviation of the liquid surface from the still surface. *PlanetWaves* is written in MATLAB and adapted from Hayes et al. (2013), which derives its framework from the University of Miami Wave Model (UMWM) (Donelan et al., 2012), written in FORTRAN. The components of the model and an example run are shown in Figure 3, Figures S1 and S8. Table S1 in Supporting Information S1 includes a table of all variables.

In the model, x and y are the horizontal coordinates in the spatial Cartesian grid with an associated depth $h(x, y)$, and ω and θ are the frequency and direction of the wave component (Figure 3a). The model produces a wavefield given the planet's liquid, atmosphere, and gravity for an imposed wind. For our investigations, the key results of interest here are the mature wave energy spectrum $E(k)$, where k is the wavenumber, and the threshold wind speed for wave generation $U_{\min}$. The model also tracks the temporal and spatial dependence of wave growth. It has been validated previously in the field and using wave tank experiments that varied liquid properties and atmospheric properties (Banfield et al., 2015; Chen & Curcic, 2016; Donelan et al., 2012; Donelan & Plant, 2009).

The main inputs to our model besides planetary conditions are the: (a) x and y dimensions and grid spacing (Δx, Δy) for a uniform grid, (b) number and spacing of discrete frequencies (Δf), (c) number of discrete directions (θ), (d) elevation at which the wind speed is specified (default $z_{\text{ref}} = 10$ m), (e) wind direction (ψ) and speed ($U_{z_{\text{ref}}}$), (f) maximum size of the time step (Δt), and (g) bathymetry $h(x, y)$. Tuneable parameters outlined in Section 2 that rely on past model estimates and laboratory experiments under terrestrial conditions are outlined in Table S2 of Supporting Information S1 and are considered provisional inputs.

In the model, the full energy balance at any location within the basin is given by

$$\frac{\partial E}{\partial t} + \frac{\partial [E[c_g \cos(\phi) + u_0]]}{\partial x} + \frac{\partial [E[c_g \sin(\phi) + v_0]]}{\partial y} + \frac{\partial [\dot{\phi} E]}{\partial \phi} + \frac{\partial [\dot{k} E]}{\partial k} = \rho g \sum_i S_i \tag{1}$$

where the wave energy density per unit area (which is commonly referred to as simply the "wave energy") spectrum is given by

$$E(x, y, \omega, \theta) = \rho g F(x, y, \omega, \theta) \tag{2}$$

and $S_i = [S_{\text{in}}, S_{\text{td}}, S_{\nu}, S_{\text{bf}}, S_{\text{wb}}, S_{\text{pb}}, S_{\text{nl}}]$, which describes the energy input from the wind and losses from turbulent dissipation, viscous dissipation, bottom friction dissipation, energy dissipation from wave breaking and white capping, energy lost from breaking at shallow depths near shore ("plunging"), and nonlinear energy transfer within the spectrum, respectively (Figure 3b). The left-hand side of Equation 1 is the material derivative of the wave energy spectrum. It consists of the local Eulerian change (first term), advection in physical space through translation (second and third terms) and rotation (fourth term), and advection in wavenumber space (i.e., refraction, fifth term).

2.1. Wave Dispersion

In the model, the wavenumbers (k) are computed from the slowest moving waves (k_0) to a maximum wavenumber ($k_{\max} = 1000$ m^{-1}) determined by the rapid dropoff in spectral density (Donelan et al., 2010, 2012;

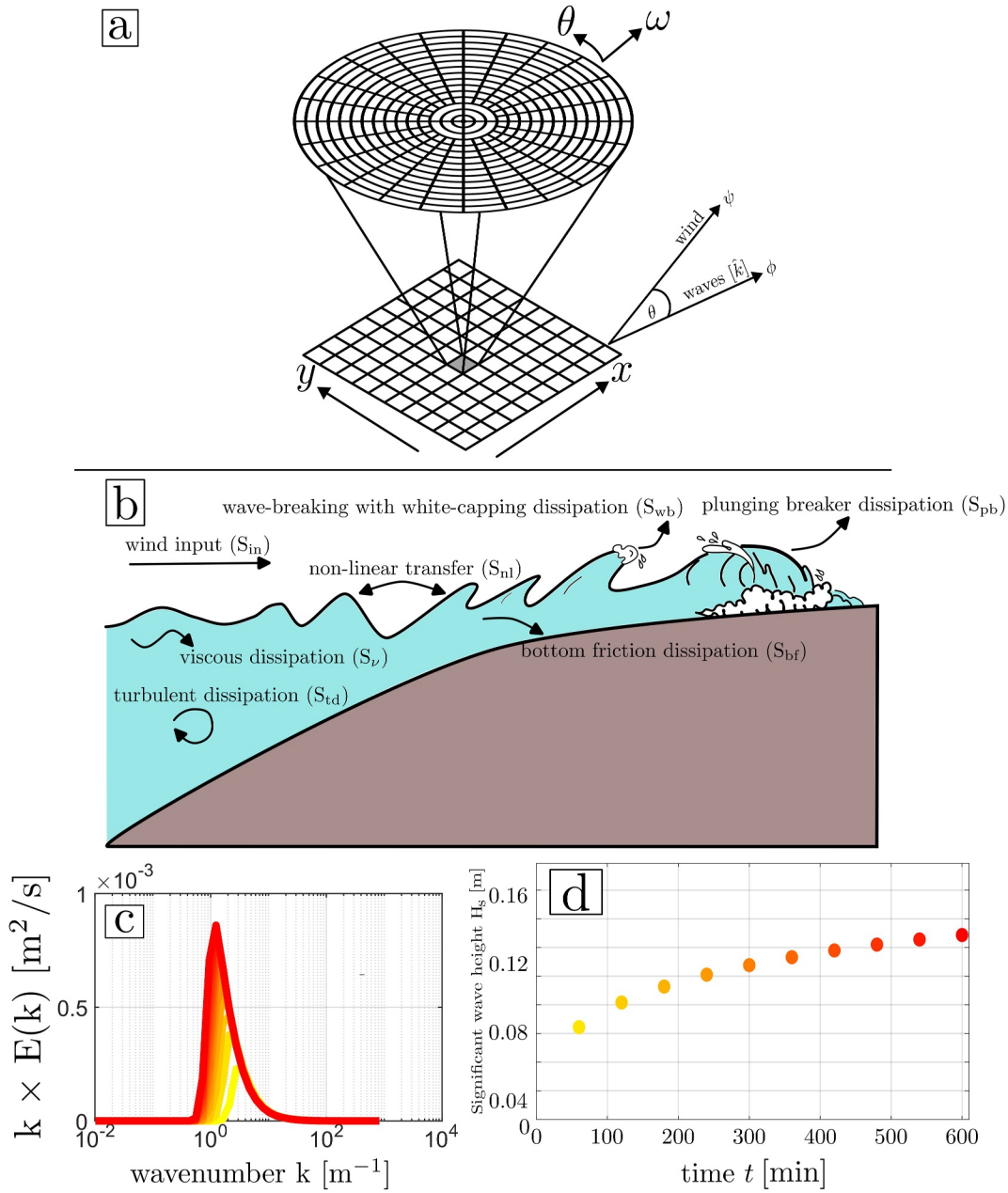

Figure 3. Wave diagram description with example. (a) Conceptual model of the four dimensional wave spectrum $F(x, y, \omega, \theta)$ where each cell (x, y) has its own distribution of power over the modeled frequency ω and direction θ components. The relative angle of wave propagation θ is the angle between the direction of the wave's propagation ϕ and the direction of the wind ψ, $\theta = \psi - \phi$, defined over the interval $[-\pi, \pi]$. For westerly winds, $\phi = 0$. (b) Schematic of input and output energy terms generating the wavefield. (c) The typical shape of the non-directional energy spectrum through time ($k\times$ (Equation 2)). (d) The significant wave height through time (Equation 42). The example shown in c-d was modeled for 3 m/s winds over 10 hr at one-minute intervals for terrestrial conditions and sampled hourly. The colors correspond to time (yellow = start time, red = end time). The spectrum in c is multiplied by wavenumber to allow the integral to be proportional to the variance of the surface height.

Figure 4b). The slowest-moving wave number (k_0) is defined by the capillary-gravity waves from linear, small-amplitude wave theory (Kinsman, 1965),

$$k_0 = \sqrt{\frac{\rho g}{\mathcal{T}}}, \tag{3}$$

21699100, 2026, 4, Downloaded from https://agupubs.onlinelibrary.wiley.com/doi/10.1029/2025JE009490 by Cochrane Russian Federation, Wiley Online Library on [30/04/2026]. See the Terms and Conditions (https://onlinelibrary.wiley.com/terms-and-conditions) on Wiley Online Library for rules of use; OA articles are governed by the applicable Creative Commons License

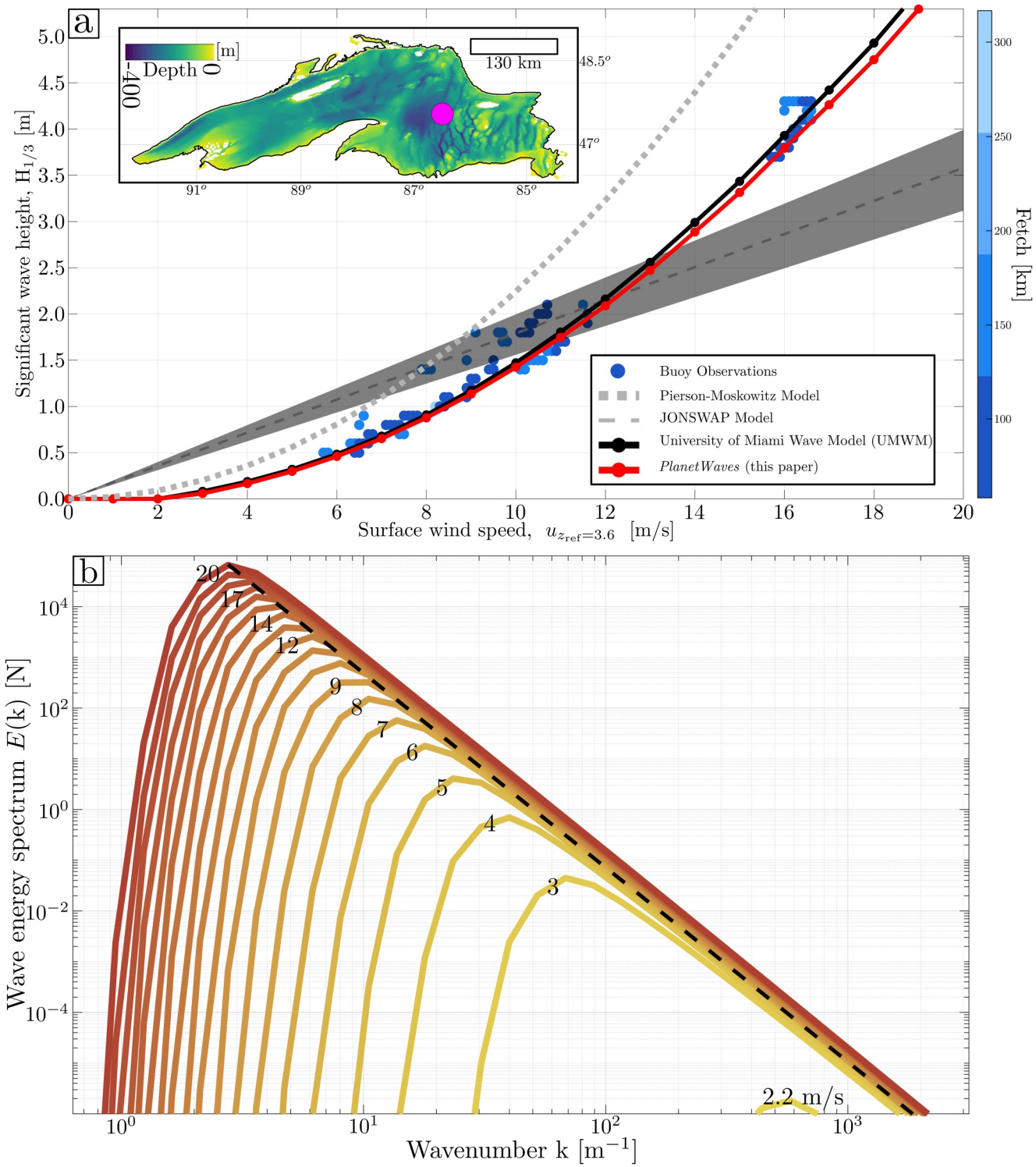

Figure 4. Comparison of models and buoy data for waves in Lake Superior at buoy 45004. (a) Significant wave height versus near-surface wind speed for wave models and buoy data. Our model (*PlanetWaves*) is shown in red. Buoy data is shown in blue with variations in hue indicating variations in fetch due to changes to the wind direction. The results for the JONSWAP model (Equation 46) are shown for average fetch (118 km) (gray, dashed) and a range within one standard deviation of the average fetch (29 km) (gray, shaded). The predictions for the Pierson-Moskowitz model (Equation 45) (gray, dotted) have no fetch dependence. The results predicted for the University of Miami Wave Model (UMWM) (Donelan et al., 2012) (black) are also shown. The inset shows buoy location (magenta) on the lake bathymetry. (b) Non-directional energy spectrum for increasing wind speed for deepwater waves after 10 model hours. The color indicates wind speed (low = yellow, high = red) with labels for magnitude ($U_{z_{ref=3.6\ m}}$ (m/s)). Dashed line is the mean power-law fit to the high frequency slope for all wind speeds: $E(k) \propto k^{-3.8}$.

21699100, 2026, 4, Downloaded from https://agupubs.onlinelibrary.wiley.com/doi/10.1029/2025JE009490 by Cochrane Russian Federation, Wiley Online Library on [30/04/2026]. See the Terms and Conditions (https://onlinelibrary.wiley.com/terms-and-conditions) on Wiley Online Library for rules of use; OA articles are governed by the applicable Creative Commons License

21699100, 2026, 4, Downloaded from https://agupubs.onlinelibrary.wiley.com/doi/10.1029/2025JE009490 by Cochrane Russian Federation, Wiley Online Library on [30/04/2026]. See the Terms and Conditions (https://onlinelibrary.wiley.com/terms-and-conditions) on Wiley Online Library for rules of use; OA articles are governed by the applicable Creative Commons License

where g is the gravitational acceleration, ρ is the density of the liquid, and $\mathcal{T}$ is the surface tension of the liquid.

The wavenumber (k) for each frequency (f) at each point on the spatial grid (x, y) is found using the linear wave dispersion relation of gravity-capillary waves for an arbitrary depth (h),

$$\omega^2 = (2\pi f)^2 = \left(gk + \frac{\mathcal{T}k^3}{\rho}\right)\tanh(kh). \tag{4}$$

The wave speed, aka celerity (c), frequency (f), and wavelength (λ) are related by $c = \lambda f$, and

$$k = \frac{2\pi}{\lambda} = \frac{2\pi f}{c} = \frac{\omega}{\sqrt{\frac{g}{k}\tanh(kh)}}, \tag{5}$$

which is solved iteratively using the Newton-Raphson method. For linearized 2D wave motion, the dispersion relation for gravity-capillary motion is given by

$$\omega^2 = c^2k^2 = \left(gh + \frac{\mathcal{T}k^2h}{\rho}\right)\left(\frac{\tanh(kh)}{kh}\right)k^2. \tag{6}$$

The phase velocity of the gravity-capillary wave is given by

$$c = \frac{\omega}{k} = \left(\frac{g}{k} + \frac{\mathcal{T}k}{\rho}\right)\tanh(kh). \tag{7}$$

The gravity-capillary wave group velocity is given by

$$c_g = \frac{d\omega}{dk} = \frac{c}{2}\left(1 + \frac{2kh}{\sinh(2kh)} + \frac{2\mathcal{T}k\rho}{\rho k} + \frac{\mathcal{T}k}{\rho}\right). \tag{8}$$

The phase velocity characterizes a single wave within the wavefield and describes the speed at which a constant phase propagates through the liquid. By comparison, the group velocity describes the dependence of frequency on wavelength within the wavefield and quantifies the propagation of the energy of wave groups. For shallow liquids ($kh \to 0$), $c_g \to c$; and for deep liquids ($kh \to \infty$), $c_g \to c/2$.

2.2. Surface Wind Drag

To estimate the energy available to the waves from the wind, we need a description of the wind at the liquid-air interface. To begin, we calculate the air density (ρ_a) at the surface using the ideal gas law,

$$\rho_a = \left(\frac{P}{RT}\right)\left(\frac{m}{\mu}\right), \tag{9}$$

where P is the surface pressure, R is the universal gas constant, T is the surface temperature, m is the mass of the gas, and μ is the number of moles of the gas.

The wind speed decreases downward through the turbulent boundary layer near the liquid surface. Assuming the atmosphere is neutrally stable (i.e., liquid and air temperature are equal), the wind speed profile can be described as a log profile (Monin & Obukhov, 1954), where the input of energy into the liquid is proportional to the curvature of the wind speed profile where wind speed is equal to the wave speed (Miles, 1957). This allows us to relate the wind velocity at the height of the free flow (U_∞) to the typical 10-m reference height $(U_z = U_{10})$. The reference scale height of interest is half the peak wavelength ($U_{\lambda/2} = U_\infty$) (Benjamin, 1959; Miles, 1957). Thus,

$$U_\infty = U_{\lambda/2} = \frac{U_*}{\kappa}\ln\left(\frac{\left(\frac{\lambda}{2}\right)}{z}\right) + U_z, \tag{10}$$

where the von Kármán constant $\kappa = 0.4$ and the height of the measured wind speed above the surface $z = 10$ m. The frictional velocity U_* is defined as the vertical flux of the horizontal momentum component of the Reynolds stress tensor, which can be expressed as a function of the net drag coefficient (C_d):

$$U_* = \sqrt{\overline{u'w'}} = U_z\sqrt{C_d}. \tag{11}$$

The initial conditions for the net drag coefficient for neutral conditions are described by (Large & Pond, 1981)

$$1000C_d = \begin{cases} 1.2 & U_{10} \le 11 \text{ m/s} \\ 0.49 + 0.065U_{10} & U_{10} > 11 \text{ m/s}. \end{cases} \tag{12}$$

There are two components to the total drag from the wind: skin drag (C_{ds}) which acts tangentially to the surface, and form drag (C_{df}), which acts normal to the surface. At low wind speeds, when the waves are small, the skin drag dominates. We define the skin drag coefficient as

$$C_{ds} = \left(\frac{U_*}{u}\right)^2 = \left(\frac{\kappa}{\log\left(\frac{z}{z_0}\right)}\right)^2. \tag{13}$$

here the momentum roughness lengthscale (z_0) for the skin drag is defined for a hydraulically smooth boundary as

$$z_0 = \frac{\nu_a}{9U_*} \tag{14}$$

where ν_a is the atmosphere's kinematic viscosity (Schlichting & Kestin, 1961).

As the wind speed increases and larger waves begin to form, the shape of the wave can shelter the lee side of the sea surface, decreasing the contribution from the skin drag (Donelan et al., 2012). For this reason, the skin drag coefficient for an arbitrary waveform (C'_{ds}) is closely related and changes as the wavefield evolves in time:

$$C'_{ds} = \frac{C_{ds}}{3}\left(1 + \frac{2C_{ds}}{C_{ds} + C_{df}}\right), \tag{15}$$

where the largest waves have an equal contribution from skin drag and form drag (Donelan et al., 2012).

The wind stress (τ) acting upon the waveform is given by

$$\tau = \rho_a U_*^2 = \rho_a C_d U_{10}^2. \tag{16}$$

To find the components of the form drag, we use the relationship between energy (E) and momentum (M), $M = \frac{E}{c}$. Shear stress (τ) is equivalent to the momentum flux ($\rho_a U_*$)U_*, which allows us to relate the components of the shear stress from the wind as

$$\tau_x = \rho_a g \int_{-\pi}^{\pi}\int_{k_0}^{k_{\max}} \frac{S_{in}}{c}\cos(\phi)\, k\mathrm{d}k\mathrm{d}\phi, \tag{17}$$

21699100, 2026, 4, Downloaded from https://agupubs.onlinelibrary.wiley.com/doi/10.1029/2025JE009490 by Cochrane Russian Federation, Wiley Online Library on [30/04/2026]. See the Terms and Conditions (https://onlinelibrary.wiley.com/terms-and-conditions) on Wiley Online Library for rules of use; OA articles are governed by the applicable Creative Commons License

$$\tau_y = \rho_a g \int_{-\pi}^{\pi} \int_{k_0}^{k_{\max}} \frac{S_{in}}{c} \sin(\phi)\, k \mathrm{d}k \mathrm{d}\phi, \tag{18}$$

where (ϕ) describes the angle of the wave's propagation (Figure 3a; Janssen et al., 2002).

The form drag coefficient is calculated as (Donelan et al., 2012)

$$C_{df} = \frac{\sqrt{\tau_x^2 + \tau_y^2}}{\rho_a U_{10}^2} \leq C_{d,\max}. \tag{19}$$

The aerodynamic roughness does not grow purely as a function of the wind speed (Donelan et al., 2004). Wave tank experiments in terrestrial conditions have shown that, for strong winds, the steep slope of the waveform separates the flow, driving the drag coefficient to asymptote near a constant value of $C_{d,\max} \approx 3 \times 10^{-3}$ (Curcic & Haus, 2020). We assume this saturation value is a constant driven by the shape of the waveform, but more work is needed to determine if it is affected by changes in the planetary conditions (Table S2 in Supporting Information S1). The stress components of the wind are then modified iteratively by this change in the skin drag coefficient (Donelan et al., 2012),

$$\tau_x = \tau_{x,0} + \rho_a C'_{ds} U_{10}^2 \cos(\psi) \tag{20}$$

$$\tau_y = \tau_{y,0} + \rho_a C'_{ds} U_{10}^2 \sin(\psi), \tag{21}$$

where ($\tau_{x,0}$) and ($\tau_{y,0}$) are defined for the previous time step using Equations 17 and 18 and (ψ) describes the angle of the wind (Figure 3a).

2.3. Energy Input From Wind

Energy to create surface waves is extracted from the wind. The input source term $S_{\text{in}}(k, \phi)$ (Figure 3b) is modeled after Jeffreys's sheltering hypothesis, which predicts that the wind separates from the liquid surface at the crest, such that the ram face of the wave experiences more pressure from the wind than the lee side. This creates a pressure gradient across the wave that allows energy to be extracted from the wind and grows the waves. When this growth exceeds the viscous damping force, capillary waves begin to form (Jeffreys, 1925). The relative velocities ($\mathcal{U}$) of interest are as follows:

$$\mathcal{U} = U_{\lambda/2} \cos\theta - c - U_d \cos\theta - u_0 \cos\phi - v_0 \sin\phi. \tag{22}$$

u_0 and v_0 are unidirectional currents that would flow even if there was no wind (e.g., tidal currents). U_d is the wind-driven current (i.e., drift velocity),

$$U_d = \frac{U_{*w}}{\kappa} \ln\left(\frac{z_k}{z_{\text{ref}}}\right), \tag{23}$$

where $z_k = 1/k$ for $z_k < z_\infty$ and $z_k = z_\infty$ otherwise. We pin the free-flow height z_∞ for the drift velocity for short wavelengths at 20 m as a provisional input (Table S2 in Supporting Information S1). The flow speed at the surface within the liquid is equal to the frictional velocity scaled by the ratio of fluid densities

$$U_{*w} = U_* \sqrt{\frac{\rho_a}{\rho}}. \tag{24}$$

The resulting input spectrum has a form where the input from the wind at any one wavenumber k is independent of the input at any other point in the spectrum (Donelan & Pierson, 1987):

21699100, 2026, 4, Downloaded from https://agupubs.onlinelibrary.wiley.com/doi/10.1029/2025JE009490 by Cochrane Russian Federation, Wiley Online Library on [30/04/2026]. See the Terms and Conditions (https://onlinelibrary.wiley.com/terms-and-conditions) on Wiley Online Library for rules of use; OA articles are governed by the applicable Creative Commons License

$$S_{\text{in}} = A_1 \mathcal{U}|\mathcal{U}|k\omega\left(\frac{\rho}{g + \mathcal{T}k^2}\right)\frac{\rho_a}{\rho}F, \tag{25}$$

where F is the spectrum of the elevation of the liquid surface relative to the still surface (η). We considered A_1 (Table S2 in Supporting Information S1) to be a function of only the wave state:

$$A_1 = \begin{cases} 0.11 & \text{wind in direction of waves and faster, } \mathcal{U} > 0 \\ 0.099 & \text{wind opposing waves, } \cos\theta < 0 \\ 0.0099 & \text{wind slower or opposing waves, } \mathcal{U} <= 0. \end{cases} \tag{26}$$

However, the value and functional form of A_1 remains an active field of study (Grare et al., 2013; Tan et al., 2023). Note, the energy input within the short ($f \geq f_{\text{diagnostic}}$; Equation 41) wavelength waves is limited as the waves approach the wind speed, so they do not drain energy from the prognostic part of the spectrum:

$$S_{\text{in}} = \mathcal{H}S_{\text{in}}, \tag{27}$$

where the Heaviside function ($\mathcal{H}$) is

$$\mathcal{H} = \begin{cases} 0 & \text{if } f \geq f_{\text{diagnostic}} \text{ and } (S_{\text{in}} < 0 \text{ or } F < 0) \\ 1 & \text{otherwise} \end{cases} \tag{28}$$

2.4. Energy Dissipation

Energy can be lost from the wavefield through several mechanisms, including–in descending order of importance–wave-breaking, turbulence, bottom friction, and viscous heating.

Early observations of ocean wave spectra undergoing wave breaking through white capping (Phillips, 1958) noted the self-similarity of the equilibrium spectral slope, in particular the falloff in power of $F\ \alpha\ k^{-4}$ for large wavenumbers (Donelan et al., 1985; Kitaigorodskii, 1983). This allows for a quantification of the wave spectrum saturation ($\mathcal{B}$) given by

$$\mathcal{B} = k^n F \tag{29}$$

where $\mathcal{B} \to 1$ for large k as the wavefield matures (Donelan et al., 2012). The asymptotic limit for fully matured waves is well-described when $n \approx 4$ (Alves et al., 2003).

As waves grow, they become steeper up to a geometric limit ($H/\lambda \gtrapprox 1/7$), and oversteepened waves will begin to break (Kinsman, 1965). For deepwater waves, wave breaking induces dissipation and, for long-wavelength waves, can entrain air and produce white capping (S_{wb}),

$$S_{\text{wb}} = -A_2\left(1 + A_3\chi^2\right)^2 \mathcal{B}^{n_b}\omega F, \tag{30}$$

where $A_3 \approx 360$ (Table S2 in Supporting Information S1) and $n_b \approx 2.5$. Because the value of n_b was determined empirically from limited field observations, we consider it a provisional input that will require further investigation to verify (Table S2 in Supporting Information S1). The coefficient A_2 is given by

$$A_2 = 0.04 + 41.96\left|2 - \frac{1 + 3\left(\frac{k}{1.15k_0}\right)^2}{1 + \left(\frac{k}{1.15k_0}\right)^2}\right|^4, \tag{31}$$

such that $A_2 \to 42$ for small frequencies (Table S2 in Supporting Information S1; Donelan, 2001).

21699100, 2026, 4, Downloaded from https://agupubs.onlinelibrary.wiley.com/doi/10.1029/2025JE009490 by Cochrane Russian Federation, Wiley Online Library on [30/04/2026]. See the Terms and Conditions (https://onlinelibrary.wiley.com/terms-and-conditions) on Wiley Online Library for rules of use; OA articles are governed by the applicable Creative Commons License

$\chi^2(k,\phi)$ is the mean square slope (MSS) in the downwind direction (ϕ) for waves with wavelength longer than $\lambda(k)$ and is given by

$$\chi^2(k) = \int_{k_p}^{k} k dk \int_{-\pi}^{\pi} F k^2 \cos^2 \phi d\phi. \tag{32}$$

The mean slope of the liquid in the direction of the shorter waves can play a role in the location and frequency of wave breaking (Equation 30). This is due primarily to hydrodynamic modulation of short waves riding on top of longer waves (Curcic, 2025; Romero, 2019). In addition, the increased slope on the lee face of longer waves increases the steepness of the shorter waves and leads to more wave breaking. Conversely, on the ram face of the longer waves, the shorter waves' slopes are decreased, helping to reduce the steepness of the shorter waves and limit wave breaking (Donelan, 2001).

As the waves enter shallow water, shoaling causes waves to rapidly steepen. A depth-dependent dissipation term captures this phenomenon, which we refer to as "plunging" breaker dissipation (S_{pb}), although this dissipation could be caused by other forms of shallow-water breaking, including spilling, collapsing, and surging

$$S_{\text{pb}} = S_{\text{wb}} \coth(\alpha k h), \tag{33}$$

where $\alpha \approx 1/5$ (Table S2 in Supporting Information S1). This treatment approximates the effects of shallow water on wave energy dissipation, but does not exactly capture the detailed and complex physics of wave breaking itself.

Additionally, the turbulent dissipation term $S_{\text{td}}(k,\phi)$ (Figure 3b) represents wave attenuation and energy loss into turbulent eddies, which favorably suppresses smaller wavelengths, and is given by

$$S_{\text{td}} = -4\upsilon_t k^2 F = -A_4 U_{*w} k F, \tag{34}$$

where υ_t is the eddy viscosity ($\nu_t \; \alpha \; U_{*w}/k$) and $A_4 = 0.0025$ (Table S2 in Supporting Information S1; Donelan et al., 2012).

The bottom friction term $S_{\text{bf}}(k,\phi)$ (Figure 3b) describes the loss of energy due to interaction with the bed and is given by

$$S_{\text{bf}} = -G_f \left(\frac{k}{\sinh(2kh)} \right) F, \tag{35}$$

where the roughness factor (G_f) varies as a function of the flow conditions and bed character (Komen et al., 1994). We assume that $G_f = 0.002$ m/s, but it can vary between 0.001 and 0.01 m/s depending on the bed roughness, which depends on particle size and, more importantly, on the presence of orbital ripples (Donelan et al., 2012).

The viscous dissipation $S_\nu(k,\phi)$, which prevents wave growth for winds below threshold, describes the loss of energy to heat by the viscosity of the liquid,

$$S_\nu = -4\nu k^2 F. \tag{36}$$

2.5. Nonlinear Energy Transfer

Energy is not just gained or lost from the wave spectrum, it can also be transferred nonlinearly between frequencies to broaden the spectrum and reduce the peak frequency, as a spectrum of nonlinear energy transfer S_{nl}. In the model, energy is transferred from a wave k to the next two neighboring longer waves ($k - \Delta k$ and $k - 2\Delta k$) as an inverse energy cascade. The amount of energy transferred to longer wavelengths falls off exponentially as the square of the frequency separation (Δf) from the donating wave, such that energy in a spectrum with smaller

21699100, 2026, 4, Downloaded from https://agupubs.onlinelibrary.wiley.com/doi/10.1029/2025JE009490 by Cochrane Russian Federation, Wiley Online Library on [30/04/2026]. See the Terms and Conditions (https://onlinelibrary.wiley.com/terms-and-conditions) on Wiley Online Library for rules of use; OA articles are governed by the applicable Creative Commons License

21699100, 2026, 4, Downloaded from https://agupubs.onlinelibrary.wiley.com/doi/10.1029/2025JE009490 by Cochrane Russian Federation, Wiley Online Library on [30/04/2026]. See the Terms and Conditions (https://onlinelibrary.wiley.com/terms-and-conditions) on Wiley Online Library for rules of use; OA articles are governed by the applicable Creative Commons License

frequency separation would be split more evenly between its neighbors (Donelan et al., 2012). The energy transfer spectrum is

$$S_{\mathrm{nl}} = A_5\left(b_1 S_{\mathrm{wb}}(k-\Delta k,\phi) + b_2 S_{\mathrm{wb}}(k-2\Delta k,\phi) - S_{\mathrm{wb}}(k,\phi)\right). \tag{37}$$

The amount of energy transferred from k is proportional by A_5 to the amount of energy dissipated by the wave breaking and white capping (Equation 30). A_5 is given by:

$$A_5 = \frac{1}{\beta}\left(\frac{C_1}{e^{\Delta f}}\right)^{C_2} \tag{38}$$

where the constants C_1 and C_2 are approximately equal to 1 and 2, respectively (Table S2 in Supporting Information S1), and

$$\beta = b_1\left(1-\frac{1}{e^{2\Delta f}}\right) + b_2\left(1-\left(\frac{1}{e^{2\Delta f}}\right)^2\right). \tag{39}$$

This transfer occurs at each wavenumber and is conservative with respect to energy in the spectrum as a whole. This results in an accumulation of energy at longer wavelengths at the expense of shorter wavelengths. For this paper, we consider a logarithmically spaced frequency distribution such that $A_5 \approx 3.2$ (Donelan et al., 2012). The coefficients (b_1, b_2) modulating the magnitude of this effect are given by

$$b_1 = 1 - b_2 = \exp\left(-C_3\left(\frac{\Delta f}{f}\right)^2\right), \tag{40}$$

where $C_3 = 16$ (Table S2 in Supporting Information S1).

2.6. Wave Propagation

Wave energy is carried across the spatial grid by the propagation of the waves. The advection term in the time-evolution of the energy spectrum is solved through an explicit upwind finite element scheme (Donelan et al., 2012). We only advect low-frequency waves and assume that the short waves reach equilibrium with the wind climate instantaneously to generate the initial roughness, delineating the high-frequency tail as the diagnostic section of the spectrum (Young, 2020). This frequency boundary is chosen to balance the competing effects of computational efficiency and numerical artifacts like ringing, and is estimated as

$$f_{\mathrm{diagnostic}} = \frac{2.12g}{U_{10}}, \tag{41}$$

which is simply four times an Earth-based estimate of the peak frequency (Pierson-Moskowitz peak frequency) (Donelan et al., 2012; Hasselman et al., 1973). To address any remaining numerical artifacts, when numerical ringing is detected in the time evolution of the significant wave height, we take the average of the final tenth of the wave growth time series. We impose the boundary condition that the wave spectrum is zero for all ω and θ at all subaerial points. Because the wind field is held constant through time and space in this paper, we focus on predictions for waves produced under stationary wind climates.

2.7. Growing and Mature Wave Field Properties

To solve for energy evolution within the basin, we integrate Equation 1 forward in time, starting from a still surface ($\eta = 0$). Δt is fixed but built up incrementally in dynamic substeps to ensure that the variance spectrum grows by a finite amount to stably draw F toward the steady-state solution.

The resulting wavefield can be described by characteristic features like the peak period (T_p) and the significant wave height (H_s). H_s– the average height of the tallest $\frac{1}{3}$ of waves, as measured from crest to trough–is diagnostic

of the total energy within the spectrum. The significant wave height is a function of the zeroth moment (m_0) of the surface elevation spectrum (F),

$$H_s = 4\sqrt{m_0}, \tag{42}$$

where m_0 describes the variance of the liquid height:

$$m_0 = \frac{1}{2\pi}\int_{\omega_{\min}}^{\omega_{\max}} F d\omega. \tag{43}$$

The peak spectral frequency f_p is estimated as the weighted mean across the entire spectrum (Young, 1995),

$$f_p = \frac{1}{T_p} = \frac{\int_0^{2\pi}\int_{f_{\min}}^{f_{\max}} f E^5\, df d\theta}{\int_0^{2\pi}\int_{f_{\min}}^{f_{\max}} E^5\, df d\theta}, \tag{44}$$

where T_p is the associated peak period within the spectrum.

2.8. Wave Model Summary

Our model (Figure 3b) inputs energy from the wind into the liquid surface at small wavelengths (Equation 25). That energy is then conservatively moved through nonlinear transfer within the spectrum to longer wavelengths (Equation 37). Energy is lost through a combination of wave breaking (Equations 30 and 33), turbulence (Equation 34), viscosity (Equation 36), and interaction with the bed (Equation 35). Over time and fetch, a stationary energy spectrum is created (Equation 1, Figure 3c) with a characteristic wave height (Equation 42, Figure 3d) and peak frequency (Equation 44).

3. Model Validation on Earth

To validate our model, we hindcasted 20 years (2002–2022) of wind wave heights using a deepwater buoy in Lake Superior (45004) from NOAA's National Data Buoy Center (NDBC). Because this paper is primarily concerned with a stationary wind climate, we only included wave heights measured during relatively homogeneous periods of time. We defined this as any 10-hr windows when: (a) the wind magnitude varied by less than 3 m/s, (b) the wind direction varied by less than 15°, and (c) the gusts did not exceed 150% of the average wind speed. Ten hours corresponds to a timescale for the group velocity of the highest frequency (i.e., the slowest; Equation 8) waves considered in this model (0.05 Hz) to fully traverse the largest fetch (356 km). These criteria were also flexible enough to allow for data coverage up to 20 m/s winds. The majority of our waves were generated by winds coming from the East, with an average fetch of 118 ± 29 km.

We ran the model with a maximum time-step of 1 minute for a total model runtime of 10 hr. We included 50 discrete frequencies, logarithmically spaced between 0.05 and 35 Hz over 72 discrete directions evenly spaced between 0 and 2π. We modeled the bathymetry as a uniform depth of 273.5 m, which corresponded to the liquid column depth below the buoy. The anemometer height of the buoy was 3.6 m above the still-water surface. The liquid and atmospheric properties were modeled after Earth conditions in Table 1. The spatial grid was a 12 × 12 grid of 20 × 20 km cells, which corresponds to a buoy with a fetch of 120 km at the center of the grid. We performed a separate model run for each discrete wind speed.

To assess the accuracy of our model, we compared our results to the UMWM and to two often-used empirical predictions for wave height: the Pierson-Moskowitz model (Pierson & Moskowitz, 1964),

$$H_s = 0.22\frac{U_{10}^2}{g}, \tag{45}$$

and the JONSWAP model (Hasselman et al., 1973),

21699100, 2026, 4, Downloaded from https://agupubs.onlinelibrary.wiley.com/doi/10.1029/2025JE009490 by Cochrane Russian Federation, Wiley Online Library on [30/04/2026]. See the Terms and Conditions (https://onlinelibrary.wiley.com/terms-and-conditions) on Wiley Online Library for rules of use; OA articles are governed by the applicable Creative Commons License

Table 1
Atmosphere and Liquid Properties for Earth, Past Mars, Past/Present Titan, and Exoplanets (Angelo et al., 2017; Cadieux, Doyon, et al., 2024; Cadieux, Plotnykov, et al., 2024; Hu et al., 2024; Steckloff, 2020; Thomson, 1996)

		Earth	Paleo-mars	Modern Titan	Past Titan	Kepler 1649-b	LHS 1140-b	55 Cancri-e
	Type	–	–	–	–	Exo-Venus	Cool Super-Earth	Hot Super-Earth
	Liquid	water	water	$0.47CH_4 + 0.40C_2H_6 + 0.13N_2$	N_2	H_2SO_4	H_2O	Andesite
	Atmosphere	N_2	CO_2	N_2	N_2	CO_2	N_2	CO_2
Input	ρ [kg/m^3]	998.21	998.21	588.15	807.22	1,838.1	998.21	2450
	ν [m^2/s]	1.2×10^{-6}	1.2×10^{-6}	8.08×10^{-7}	1.9×10^{-7}	3.4×10^{-5}	1.2×10^{-6}	1.29×10^{-3}
	ν_a [m^2/s]	1.46×10^{-5}	1.6×10^{-5}–3.94×10^{-6}	1.16×10^{-6}	1.38×10^{-6}	7.78×10^{-6}	1.48×10^{-5}	1.48×10^{-4}
	g [m/s^2]	9.81	3.71	1.352	1.352	8.87	18.4	22.7
	T [K]	288	288	92	77.5	288	288	1,500
	P [kPa]	101.3	50–200	152	90.2	101.3	99.99	99.99
	$\mathcal{T}$ [N/m]	0.074	0.074	0.033	0.0088	0.053	0.074	0.43
	$\frac{m}{\mu}$ [kg/mol]	0.028	0.044	0.028	0.028	0.044	0.028	0.044
	ρ_a [kg/m^3]	1.18	0.92–3.68	5.56	3.92	1.86	1.17	0.35
Output	U_{min} [m/s]	2.2	1.2–1.7	0.6	0.5	5.3	2.7	37.1
	H_s at U_{10} = 5 m/s [m]	0.3	0.7–1.4	5.0	3.9	0.0	0.2	0.0
	T_p at U_{10} = 5 m/s [s]	3.0	6.7–8.5	25.3	22.2	-	1.7	-

Note. Values for molten rock are modeled after Mount Hood Andesite (~60% SiO_2 17% Al_2O_3 6% CaO) at 1500°C in air (Murase & McBirney, 1973). The final calculated wind speed threshold for wave generation (U_{min}), significant wave height (H_s), and peak wave period (T_p) after 10 hr of constant 5 m/s winds on different planets are also included for reference (Figure 8).

$$H_s = 4\sqrt{\left(1.67 \times 10^{-7}\right) \frac{U_{10}^2}{g} X}, \tag{46}$$

where X is the fetch in meters.

As expected, we find that large wind speeds have a smaller peak wavenumber (k_p), and more energy per unit length ($\int kE(k)dk$) is contained within the wavefield. For large wavenumbers ($k/k_p \gg 1$), the energy spectra collapses toward a simple power law k^{-n} and no longer depends on wind speed (Figure 4). We find an RMS error in the fit between the significant wave heights measured by the buoy and our modeled wave heights of 0.23 m. Some of this error is likely due to scatter within the data due to non-stationary characteristics of the local climate not modeled here (i.e., changes to the wind's direction, magnitude, and gustiness) (Figure 4a). This is comparable to the error of 0.20 m of the UMWM and less than the error of 0.68 and 1.03 m for JONSWAP and Pierson-Moskowitz respectively.

Waves are predicted to begin growing for wind speeds greater than 2.2 m/s, which is consistent with previous estimates of wind speed thresholds from field and laboratory measurements (~0.6–2.2 m/s) (Donelan & Pierson, 1987; Kahma & Donelan, 1988). We also retrieve the expected shape of the spectrum without prescribing it as a starting condition and instead only through solving the energy balance in Equation 1 (Figure 4b). Specifically, we see a peaked energy spectrum where the peak wavelength (k_p) shifts to shorter frequencies with higher wind speeds, with a high frequency slope that is a simple power law k^{-n} with no wind speed dependence (Figure 4b and Equation 29). We fit a regression line to our high frequency slope and find a mean n of 3.8 ± 0.05. From Equation 29, when $n \approx 4$ the waves are fully matured. This suggests we are close to complete saturation. This high-frequency slope also falls within the range previously reported within the Great Lakes (Liu, 1989). The shape stabilization is driven by the nonlinear term (Equation 37), which approximates the self-stabilizing resonant wave-wave interaction within the spectrum (Hasselman et al., 1973).

21699100, 2026, 4, Downloaded from https://agupubs.onlinelibrary.wiley.com/doi/10.1029/2025JE009490 by Cochrane Russian Federation, Wiley Online Library on [30/04/2026]. See the Terms and Conditions (https://onlinelibrary.wiley.com/terms-and-conditions) on Wiley Online Library for rules of use; OA articles are governed by the applicable Creative Commons License

21699100, 2026, 4, Downloaded from https://agupubs.onlinelibrary.wiley.com/doi/10.1029/2025JE009490 by Cochrane Russian Federation, Wiley Online Library on [30/04/2026]. See the Terms and Conditions (https://onlinelibrary.wiley.com/terms-and-conditions) on Wiley Online Library for rules of use; OA articles are governed by the applicable Creative Commons License

The results also agree well with estimates made by the original UMWM (Figure 4 and Figure S2 in Supporting Information S1), which suggests that the modifications to the model to allow them to generalize to other planetary conditions does not substantially affect the accuracy of the final predicted wave height. The small variation between predicted modeled wave heights (Figure S2 in Supporting Information S1) can be explained by two primary effects. (a) Equation 31's dependence on the value of k relative to the smallest wavenumber k_0 varies from the assumption in UMWM that A_2 is a constant of 42 for all frequencies (Donelan et al., 2012). For larger A_2 and A_3 values, the spectrum is more peaked because shorter waves are preferentially dissipated as longer waves dilate and compress shorter waves as they pass. (b) The dependence of A_5 in Equation 38 on the frequency separation Δf varies from the assumed constant value of $A_5 = 5$ in UMWM. Ultimately, the values of these coefficients vary among models and are typically chosen to fit a measured wavefield. They are therefore considered provisional inputs to the model (Table S2 in Supporting Information S1) where the effect on the final predicted wave height is minor (Figure 4 and Figure S2 in Supporting Information S1). In other words, our model remains both accurate with respect to buoy measurements and consistent with respect to previous terrestrial wave models.

4. Application to Planetary Conditions

We applied the numerical wave model *PlanetWaves* to three scenarios of interest in planetary science: past Mars, past/present Titan, and possible exoplanetary oceans. Among these scenarios, gravity, liquid, and atmospheric properties varied (Figure 2 and Table 1). We focused this investigation on the predicted threshold wind speed to generate gravity-capillary waves, as well as how the relationship between the significant wave height and peak wave period as wind speed changed across variable planetary conditions.

4.1. Paleo-Mars: Jezero Crater Lake

We modeled waves within Jezero crater (Figure 1b). For the shape and depth of the lake, we used the mosaic digital terrain model (DTM) assembled from observations by the Mars 2020 Perseverance mission and the Mars Reconnaissance Orbiter (MRO) (Mangold et al., 2021). For computational efficiency, we degraded the grid resolution from 20 to 2,000 m/pixel using a bicubic interpolation to generate a weighted average over the nearest 4×4 neighbors. We set the water level to the topset breakpoint in the Kodiak butte, which has been interpreted as a fragment of the western delta fan formed within Jezero crater (Mangold et al., 2021, 2024). This yields a maximum depth of 10 m. It should be noted that the lake level is believed to have changed through Martian history (Mangold et al., 2024), and some of this is recorded within the Kodiak butte itself, so our choice of depth is meant as only one possible lake level and not representative of the entire formation time of the Jezero delta. This choice of depth also allows a more direct comparison with the results of Rubin et al. (2022) in the Gale crater lake (Figure S5 in Supporting Information S1). Our approach disregarded the effects of subsequent aeolian or chemical erosion that could have altered the depth of the crater in the time since liquid water was present on the surface.

We considered a purely easterly (i.e., coming from the east) wind blowing for 10 hr. We modeled at a maximum resolution of 1 min. We report the wave climate at the western fan, which has 45 km fetch. We included 50 discrete frequencies, logarithmically spaced between 0.05 and 35 Hz over 72 discrete directions between 0 and 2π. The liquid and atmospheric properties were modeled after Mars conditions in Table 1 for a 50 kPa atmospheric pressure scenario (Hu & Thomas, 2022; Rubin et al., 2022; Wordsworth, 2016). The Perseverance Mars Environmental Dynamics Analyzer (MEDA) instrument directly measured wind speeds up to approximately 20 m/s at the Jezero crater floor through Northern spring and summer, with short gusts of up to 25 m/s (Viúdez-Moreiras, De La Torre et al., 2022; Viúdez-Moreiras, Lemmon, et al., 2022). Past climate models for thinner (0.5 kPa) atmospheres have produced temperature gradients comparable to modern-day Mars (Mischna et al., 2000). However, a thicker past atmosphere may have resulted in slower winds, so we considered wind speeds up to only 10 m/s for Figure 5. For faster wind speeds, see Figure 8. To investigate the effect of changing atmospheric pressure, we also repeated the model runs at a higher atmospheric pressure (200 kPa) (Figure 5e). Because the atmospheric density is calculated using the atmospheric pressure (Equation 9), this produces atmospheric densities of 0.92 kg/m^3 and 3.68 kg/m^3 for the 50 and 200 kPa, respectively. The surface pressure range was inferred from cratering records and nitrogen and argon isotopic compositions in the modern-day Martian atmosphere (Kite et al., 2014; Kurokawa et al., 2018).

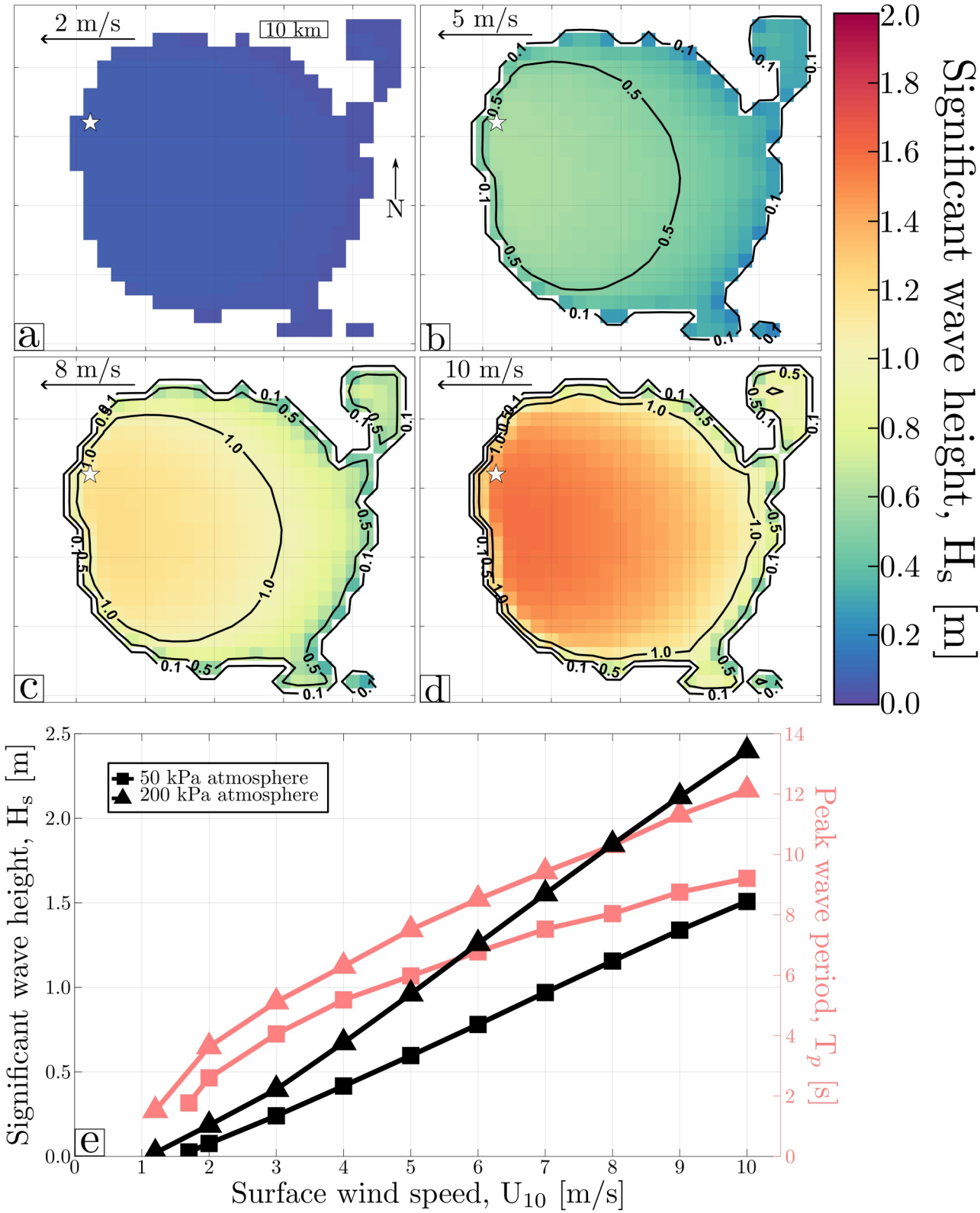

Figure 5. Modeled waves at Jezero crater, Mars. (a–d) Significant wave heights as a function of wind speed for easterly (arrow) winds between 0 and 10 m/s. Contours are wave height (m). (e) Wave heights at western fan (at the starred location in panels (a–d) and peak wave periods as a function of the surface wind speed and atmospheric surface pressure from 50 kPa (a–d) and 200 kPa. Intermediate wind speeds are included in the (Videos S9 and S10).

21699100, 2026, 4, Downloaded from https://agupubs.onlinelibrary.wiley.com/doi/10.1029/2025JE009490 by Cochrane Russian Federation, Wiley Online Library on [30/04/2026]. See the Terms and Conditions (https://onlinelibrary.wiley.com/terms-and-conditions) on Wiley Online Library for rules of use; OA articles are governed by the applicable Creative Commons License

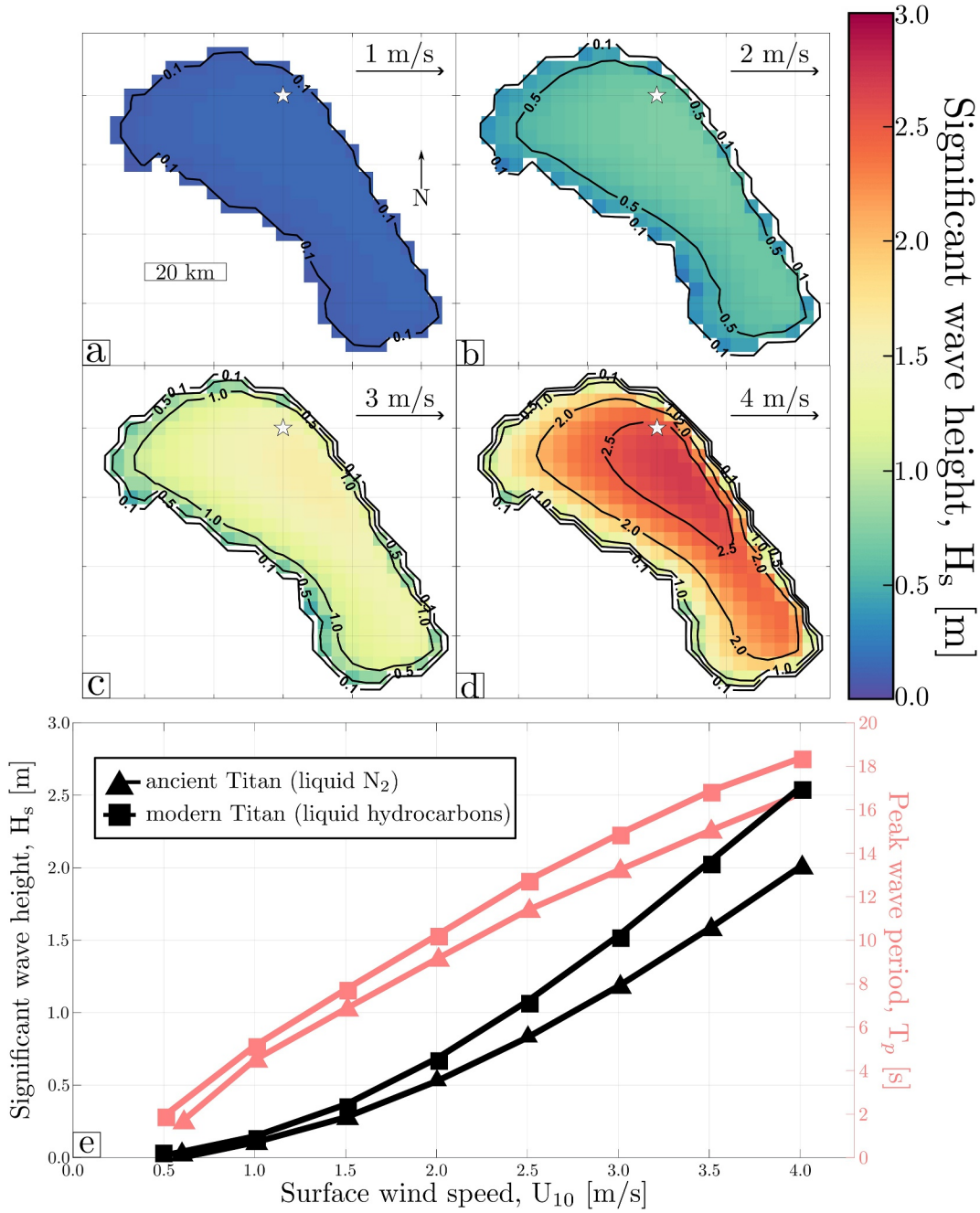

Figure 6. Modeled waves at Ontario Lacus, Titan. (a–d) Significant wave heights as a function of wind speed in Ontario Lacus for liquid hydrocarbon lakes for westerly (arrow) winds. (e) Nearshore significant wave height and peak wave periods within the lake (at starred location in panels (a–d) as a function of wind speed and liquid properties (liquid hydrocarbons vs. liquid N_2 in possible paleo-Titan conditions). Intermediate wind speeds are included in the (Videos S11 and S12).

We find that waves begin to grow at a threshold wind speed of 1.7 m/s for a 50 kPa atm and 1.2 m/s for a 200 kPa atm, which is less than the wind speed threshold of 2.2 m/s for waves at Lake Superior on Earth at 1.013 bar. The peak wave period is also shorter across all modeled wind speeds for a 50 kPa atm, with the difference increasing to 2.9 s at 10 m/s (Figure 5e). At all modeled wind speeds, the resulting wave heights increase with increased fetch (Figures 5a–5d), suggesting that the size of the crater is an important constraint on the wave energy imparted into the past shoreline. For example, for 10 m/s easterly winds, the wave heights nearest to the east coast are ∼0.5 m, compared to the west coast that experiences waves ∼1.5 m waves (Figures 5a–5d).

21699100, 2026, 4, Downloaded from https://agupubs.onlinelibrary.wiley.com/doi/10.1029/2025JE009490 by Cochrane Russian Federation, Wiley Online Library on [30/04/2026]. See the Terms and Conditions (https://onlinelibrary.wiley.com/terms-and-conditions) on Wiley Online Library for rules of use; OA articles are governed by the applicable Creative Commons License

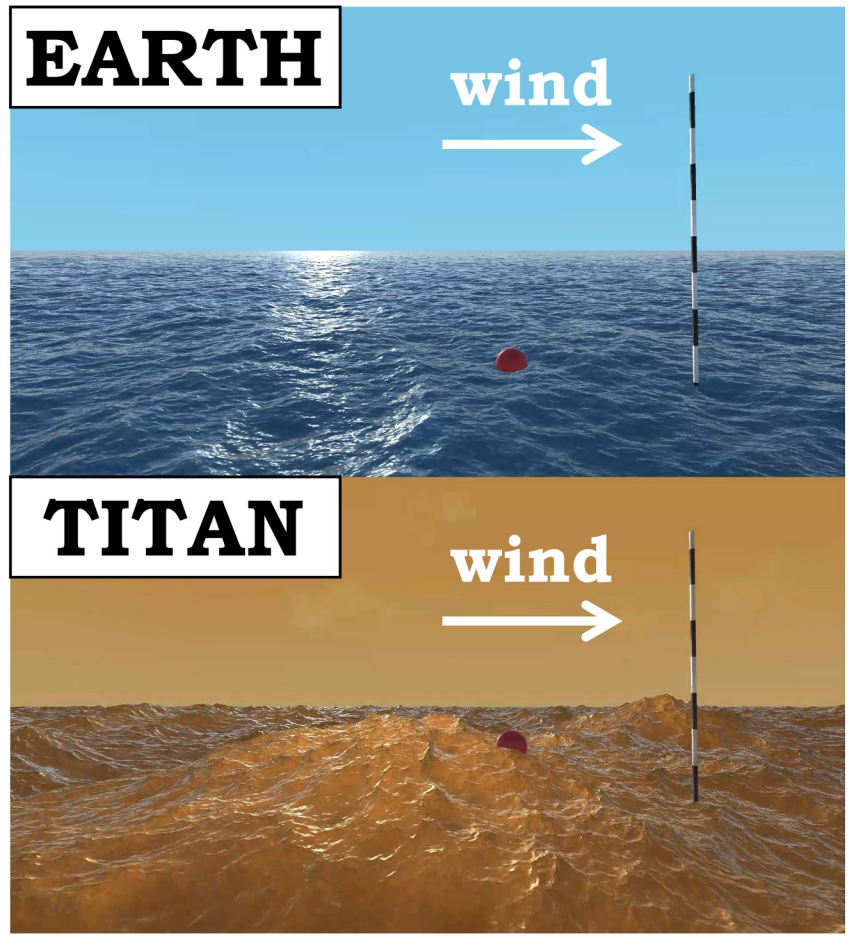

Figure 7. Perspective view of waves on Earth and Titan based on numerical simulations with a 4 m/s wind coming from the left. For scale, the red sphere is 1 m in diameter and the stripes are 1 m wide. (top) Waves under Earth conditions have a significant wave height of 0.2 m. (bottom) Waves under Titan conditions have a significant wave height of 3.3 m. Videos S13 and S14 illustrates how waves on Titan move more slowly than those on Earth, primarily due to Titan's weaker gravity.

The lower atmospheric pressure also produces smaller waves across the entire range of modeled wind speeds compared to the denser atmosphere (Figure 5e). The increase in significant wave height for increased atmospheric pressure decreases for faster surface winds, with wave heights of 0.08 and 0.18 m under 50 and 200 kPa for 2 m/s winds respectively, and from 1.5 to 2.4 m for winds of 10 m/s (Figure 5e).

4.2. Titan: Ontario Lacus

We modeled Ontario Lacus (Figure 1a) to test the hypothesis that the lack of measured wave activity (Grima et al., 2017; Wye et al., 2009; Zebker et al., 2014) was due to a combination of instrumental resolution limits and weak winds (Hayes et al., 2013; Mitchell & Lora, 2016). We used a 24 × 27 grid of 3.3 × 3.3 km cells of bathymetry inferred from the calibrated SAR-brightness measured by *Cassini* (Hayes, 2016). We applied an easterly near-surface wind, consistent with previous in situ observations (Folkner et al., 2006) and global climate models (Olim et al., 2025). The liquid was modeled as a tertiary mixture of 47% methane, 40% ethane, and 13% dissolved N_2 at Titan conditions in Table 1 (Hayes, 2016; Nixon, 2024; Steckloff, 2020). We also investigated the dependence of wave height on composition by considering a possible paleo-Titan environment where the surface temperature dropped precipitously due to methane depletion and allowed liquid nitrogen (Table 1) to condense into surface lakes (Charnay et al., 2014; Lorenz et al., 1997).

We find that waves on past and present Titan appear at lower wind speeds (0.5–0.6 m/s) and grow to larger heights for a given wind speed compared to waves on Earth (Figures 6–8), which agrees with previous empirical estimates

21699100, 2026, 4, Downloaded from https://agupubs.onlinelibrary.wiley.com/doi/10.1029/2025JE009490 by Cochrane Russian Federation, Wiley Online Library on [30/04/2026]. See the Terms and Conditions (https://onlinelibrary.wiley.com/terms-and-conditions) on Wiley Online Library for rules of use; OA articles are governed by the applicable Creative Commons License

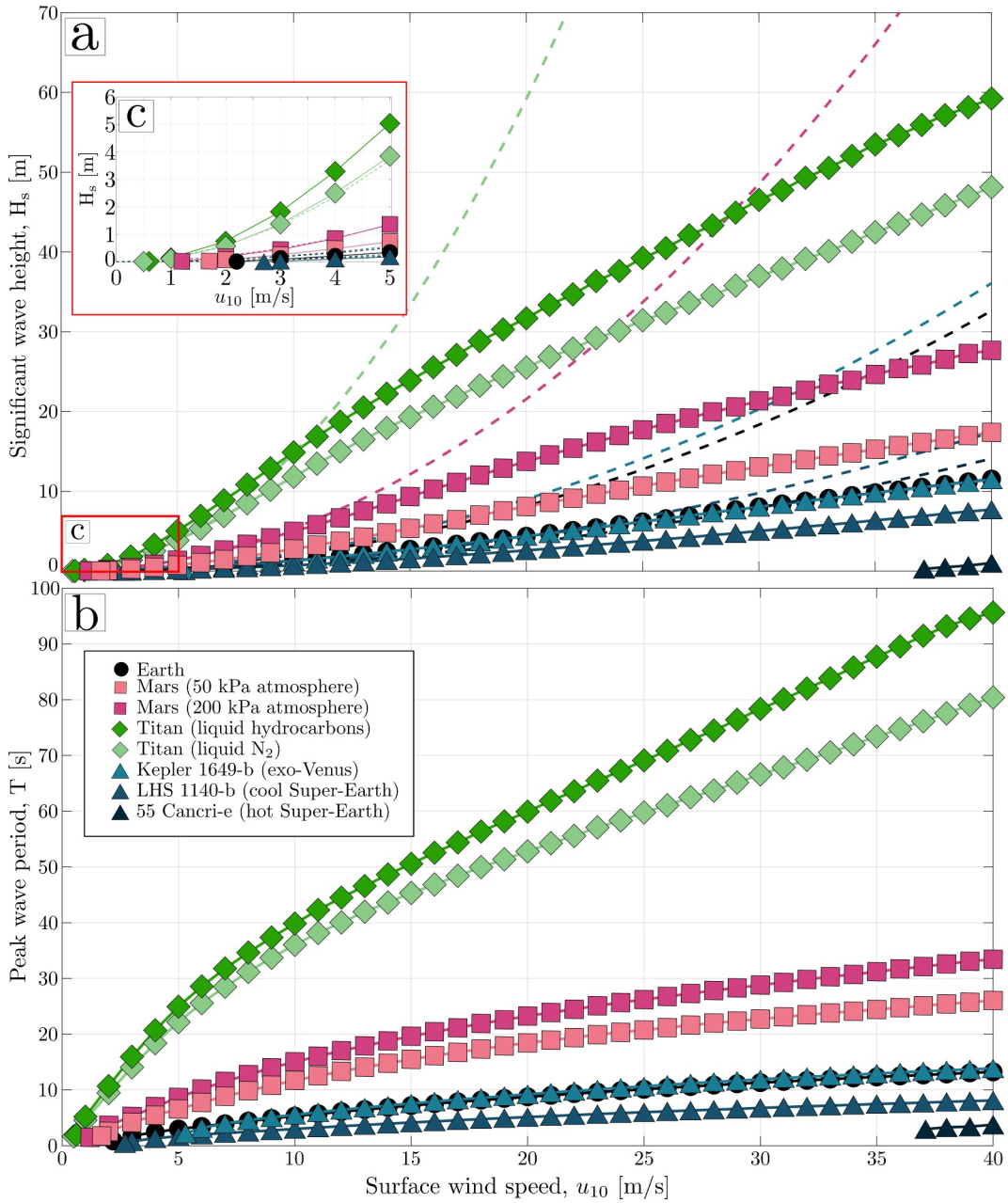

Figure 8. Modeled waves across different planetary conditions. (a) Wave formation threshold and significant wave height as a function of surface wind speed for a variety of planets and exoplanets. Dashed lines are predictions for wave height from the parabolic terrestrial model (Equation 45) (b) Peak wave period as a function of surface wind speed. (c) Inset showing details of (a) for weak surface winds most relevant to Titan conditions (<5 m/s) (Lora et al., 2022).

(Lorenz et al., 2005, 2010; Lorenz & Hayes, 2012) and modeled estimates (Hayes et al., 2013). The composition influences both the threshold wind speed, peak wave period, and the wave height (Figure 6e). Waves in liquid hydrocarbon lakes are taller and require slightly faster winds to begin to grow (0.6 m/s) compared to liquid N_2 (0.5 m/s), with the difference in wave height increasing for faster surface wind speeds (Figure 6e). The peak wave periods are also longer for Titan's lakes compared to the same wind speeds on Earth. These waves are also slower-moving compared to Earth, mostly due to reduced gravity, but also with a weak dependence on composition (Figures 7 and 8). For 4 m/s winds, this translates to a difference in peak wave period of 1.6 s for waves on a modern versus ancient Titan surface.

21699100, 2026, 4, Downloaded from https://agupubs.onlinelibrary.wiley.com/doi/10.1029/2025JE009490 by Cochrane Russian Federation, Wiley Online Library on [30/04/2026]. See the Terms and Conditions (https://onlinelibrary.wiley.com/terms-and-conditions) on Wiley Online Library for rules of use; OA articles are governed by the applicable Creative Commons License

21699100, 2026, 4, Downloaded from https://agupubs.onlinelibrary.wiley.com/doi/10.1029/2025JE009490 by Cochrane Russian Federation, Wiley Online Library on [30/04/2026]. See the Terms and Conditions (https://onlinelibrary.wiley.com/terms-and-conditions) on Wiley Online Library for rules of use; OA articles are governed by the applicable Creative Commons License

4.3. Exoplanet Lakes or Oceans

The presence of waves on the surface of a liquid changes the characteristics of the measured scattered light (Zugger et al., 2010). This may allow the presence of exoplanet lakes or oceans to be inferred remotely. The broad variety of exoplanets already observed (Wordsworth & Kreidberg, 2022) and the stability of different materials for different pressure-temperature regimes (Figure 2) allow these exoplanets to potentially be home to exotic surface liquids. The details of these exoplanets are currently speculative. In this work, we are primarily interested in how changes to planetary conditions change the generation and characteristics of surface waves. These possible exoplanetary oceans simply provide an evocative framework to explore this parameter space, and the planetary parameters (Table 1) may need to be adjusted as more information becomes available.

We explored three scenarios (Table 1): (a) the exo-Venus Kepler 1649-b with a possible hydrogen sulfide ocean, which serves as a useful analogue to past or future Venus (Angelo et al., 2017), (b) a super-Earth (LHS 1140-b) with a liquid water ocean (Cadieux, Doyon, et al., 2024; Cadieux, Plotnykov, et al., 2024), and (c) a super-Earth (55 Cancri-e) hot enough to sustain a liquid rock ocean (Hu et al., 2024). For this work, we disregarded any tidal effects from the host star and companion planets.

We report the significant wave height and peak wave period at the center of a 10 × 10 grid with 20 km point spacing (100 km fetch) with a uniform depth of 100 m after 10 hr with a maximum time step of one minute for surface wind speeds between 0.1 and 40 m/s (Figure 8). We included 100 discrete frequencies, logarithmically spaced between 0.01 and 35 Hz over 8 discrete directions between 0 and 2π.

We find that the exo-Venus Kepler 1649-b's liquid sulfuric acid oceans have a high threshold for wave generation (5.3 m/s) compared to Earth (Figure 8a and Table 1). However, for winds exceeding this threshold, the wave height is nearly identical to waves on Earth due to the planet's similar gravity. LHS 1140-b's liquid water ocean begins to grow for winds exceeding 2.7 m/s, a slightly higher threshold than Earth (Figure 8a and Table 1). The larger gravity also reduces the significant wave height relative to Earth (Figure 8a). The liquid rock oceans of 55 Cancri-e have the highest wind speed threshold (37.1 m/s) due primarily to their high surface tension and large gravity (Figure 8b and Table 1). The peak wavelengths for Kepler 1649-b and LHS 1140-b increase over two orders of magnitude as the surface wind speed increases from threshold to 40 m/s (1.9–197.3 m and 6.6–255.6 m for LHS 1140-b and Kepler 1649-b, respectively (Figure S7 in Supporting Information S1)). In addition, for each planet, wave growth varies spatially across the large, closed basin (Figure S3 in Supporting Information S1).

5. Discussion

5.1. Waves on Mars

Due to Mars' weaker gravity, waves begin to form for weaker threshold winds when compared to waves formed on Earth within the same bathymetry and for the same fetch. The sensitivity of wave height to atmospheric pressure (Figures 5 and 8) also suggests that the size of the waves would have decreased substantially as the atmospheric pressure decreased through Mars' evolutionary history. For a drop in atmospheric pressure from 200 to 50 kPa, the final wave height decreases by 60%–65% for wind speeds between 3 and 10 m/s, with the percent change decreasing for faster wind speeds (Figure 5e). We also find that the growth of the waves is affected by a change to the atmospheric pressure, where the threshold wind speed on Mars at 200 kPa was lower (1.2 m/s) than at 50 kPa (1.7 m/s) (Figure 5 and Table 1), with smaller waves corresponding to a weaker surface pressure (Figure 5b). This suggests that a lower atmospheric pressure in Mars' past could have led to a smaller wavefield overall. However, a weaker atmospheric pressure could have also driven stronger winds for the same temperature gradient, which complicates a direct comparison. If crater lakes or hemispheric oceans were stable on Mars' surface today, the lower pressure would create a higher wind speed threshold for wave formation (2.1 m/s), and the resulting waves would be shorter (Figure S4 in Supporting Information S1).

Our wave predictions can be directly compared with prior Martian studies using terrestrial or semi-empirical models. Adams (2023) applied deep-water empirical relationships and predicted ∼2 m waves for Gale crater (10 m/s wind, 10 m depth, 50 km fetch, terrestrial pressure) versus our 1.5–2.4 m and found longer fetch dependence before saturation. Their terrestrial scaling diverges more under Martian conditions, (e.g., 2–4 s shorter periods (Figure S6 in Supporting Information S1)). Using SWAN with reduced pressure and finite depth, Rubin et al. (2022) predicted 2.5 m waves within Gale crater. Under the same conditions, our model predicts 2.7 m (Figure S5 in Supporting Information S1). By contrast, Kraal et al. (2006), who used the Pierson–Moskowitz

21699100, 2026, 4, Downloaded from https://agupubs.onlinelibrary.wiley.com/doi/10.1029/2025JE009490 by Cochrane Russian Federation, Wiley Online Library on [30/04/2026]. See the Terms and Conditions (https://onlinelibrary.wiley.com/terms-and-conditions) on Wiley Online Library for rules of use; OA articles are governed by the applicable Creative Commons License

spectra with terrestrial pressure and no fetch limit, predicting ∼5 m waves at 10 m/s. With reduced pressure and finite fetch, our model yields substantially smaller waves, underscoring sensitivity to atmospheric density and fetch. Our wind speed thresholds also align with flume experiments by Banfield et al. (2015), who found ∼1–2 m/s at 100 kPa (our: 1.4 m/s) and higher thresholds under reduced pressure, consistent with our results. Because Mars is similar to Earth in fluid properties, terrestrial laws with a gravity dependence can approximate wave heights. However, our model explicitly resolves atmospheric density, wind stress, fetch, and depth, avoiding Earth-based assumptions that become unreliable as the environment becomes more exotic.

5.2. Waves on Titan

On Titan, the waves begin to form for weaker wind speeds and grow much taller than waves under the same wind speeds on Earth lakes (Figures 6–8). This is due to a combination of the weaker gravity, higher atmospheric pressure, and decreased liquid viscosity of the hydrocarbons. Our finding of a wind speed threshold of 0.6 m/s is sensitive to composition (N_2 vs. hydrocarbons) (Table 1), which suggests the wave size and timing could change across different lakes, seasons, and climates. This is consistent with previous empirical and model estimates of the wavefield on Titan (Hayes et al., 2013; Lorenz et al., 2010; Lorenz & Hayes, 2012), which predicted a wind speed threshold between ∼0.4 and 1 m/s for liquid hydrocarbons.

Past work has suggested a simple relationship between wave height and surface wind speed on Titan ($H_s \approx 0.2U_{10}^2$ (Lorenz & Hayes, 2012)). While this parabolic scaling provides a reasonable approximation for Titan's significant wave height at low wind speeds (Figure 8c), it systematically overpredicts wave heights under stronger wind conditions. On Earth, for example, the same parabolic form produces a significant wave height curve that exceeds buoy observations at wind speeds of ∼20 m/s (Figure 4, Pierson–Moskowitz curve). This discrepancy indicates that Lorenz and Hayes (2012)'s assumption of viscous dissipation as the primary energy sink is insufficient to limit wave growth at moderate to high wind speeds. Because Titan's atmosphere is much denser than Earth's, the equivalent wind stress (Equation 16) is larger $\tau_{\text{Titan}} \approx 5\left(\frac{U_{10,\text{Titan}}}{U_{10,\text{Earth}}}\right)^2 \tau_{\text{Earth}}$. This scaling suggests that a wind speed of ∼20 m/s on Earth imposes stress on the liquid surface comparable to that produced by a ∼4 m/s wind on Titan. Since the parabolic relationship overpredicts waves at 20 m/s on Earth by underestimating the influence of other sources of dissipation, it likely also overpredicts waves for Titan winds near ∼4 m/s, a regime that past climate modeling has suggested could occur near Ontario Lacus (Lora et al., 2022). Furthermore, the parabolic scaling is insensitive to changes in fluid and atmospheric properties, which is inconsistent with laboratory results showing that wave growth depends strongly on liquid viscosity and atmospheric density (Banfield et al., 2015). In contrast, our model explicitly incorporates these dependencies, yielding a more physically realistic prediction.

5.3. Waves on Exoplanets

Exoplanets allow us to test extreme environments (e.g., strong gravity, high atmospheric pressure and temperature, large viscosity) that are far removed from our experience within our own solar system. The exo-Venus with sulfuric acid oceans Kepler 1649-b has a higher threshold than any solar system body, but the waves grow to comparable heights above this threshold relative to Earth for a given wind speed because of their similar gravities (Figure 8 and Table 1). This also showcases the possibility that a past or future version of our own Venus with a lower temperature and pressure could host waves. The super-Earth water world (LHS 1140-b) is similar to Earth, but the much higher gravity depresses wave development in both the threshold wind speed and resulting wave height (Figure 8 and Table 1). For the hot super-Earth 55 Cancri-e, which has both an extremely high surface temperature and an ocean of highly viscous and dense liquid rock, waves only start to grow for winds exceeding 37.1 m/s (Figure 8 and Table 1). Because the exact atmospheric density remains uncertain (Hu et al., 2024), the range of estimated surface pressures allows for a large range in predicted wind speed thresholds (for a 0.01 bar atm the threshold is predicted to be 192.5 m/s and a 1,000 bars atm has a threshold of 6.4 m/s). For the same wind speed, waves grown under the thinner atmosphere are also shorter than waves grown under the thicker atmosphere. For example, if there was a stable liquid lake of molten rock and steady surface winds of 200 m/s on 55 Cancri-e, our model would predict significant wave heights of 1.3 m under 0.01 bar, 23.6 m under 1 bar, and 245.47 m under a 1,000 bar atm. The likelihood of surface winds this high depends on the global climate of 55 Cancri-e and its proximity to its host star, which are not well-constrained at this time.

21699100, 2026, 4, Downloaded from https://agupubs.onlinelibrary.wiley.com/doi/10.1029/2025JE009490 by Cochrane Russian Federation, Wiley Online Library on [30/04/2026]. See the Terms and Conditions (https://onlinelibrary.wiley.com/terms-and-conditions) on Wiley Online Library for rules of use; OA articles are governed by the applicable Creative Commons License

6. Conclusion

We developed *PlanetWaves*, a physics-based model for wind-generated surface waves that can be applied to any planet. This model was then applied to three scenarios of interest in planetary science: past Mars, Titan, and possible exoplanetary oceans.

On Mars, we find that the lower gravity decreases the wind speed threshold to 1.2–1.7 m/s and increases the significant wave height relative to Earth (maximum of 6.2 m taller for 50 kPa and 17.4 m taller for 200 kPa for deepwater waves for winds up to 40 m/s; Figure 8). We also find that the wave growth and equilibrium height are sensitive to atmospheric pressure, with lower pressures corresponding to smaller waves (Figure 5). This suggests that the wave heights within Mars' lakes may have decreased as the atmosphere thinned, although a concurrent increase in the wind speed could have partially offset this effect.

On Titan, we find that the lower gravity, lower liquid density and viscosity, and higher atmospheric pressure can create waves at low wind speeds (0.5–0.6 m/s) that grow much taller (maximum of 50.0 m taller for hydrocarbon lakes and 38.3 m taller for liquid N_2 for deepwater waves for winds up to 40 m/s; Figure 8) and propagate more slowly than their terrestrial counterparts for a given wind speed (Figure 7). The exact threshold and size of the waves is sensitive to composition and could theoretically vary between lakes and through seasons and past climates.

We explored three distinct exoplanet scenarios: an exo-Venus with a sulfuric acid ocean (Kepler 1694-b), a super-Earth water world (LHS 1140-b) that is similar to Earth but with a much higher gravity, and a super-Earth hot enough to sustain liquid rock on its surface (55 Cancri-e). The exo-Venus Kepler 1649-b, which could represent a past or future version of our own Venus, could sustain wave heights that are comparable to Earth's because of its similar gravity but require a much higher threshold wind speed (5.3 m/s). Waves on LHS 1140-b grow smaller than on Earth's oceans for a given wind speed and require a higher wind speed threshold (2.7 m/s). The liquid rock ocean of 55 Cancri-e exhibits the highest wind speed threshold (37.1 m/s) and are shorter than the terrestrial waves by up to 10.7 m for deepwater waves for winds up to 40 m/s (Figure 8).

This work illustrates how wave action could represent an important surface process for planets with lakes and seas on their past or present surfaces. Differences in the environment, such as liquid and atmospheric properties along with gravity, strongly modulate the occurrence and energy of the waves. This suggests that while waves may theoretically be able to form under these varying conditions, the size and timescale of their effect on the surface strongly depends on the planet and liquid in which they form. The generation and size of waves could ultimately play a direct role in the modification of the surface and climate over time. In addition, the presence of surface waves can change the properties of the scattered light, which could provide new insights into the environmental conditions of distant planets.

Conflict of Interest

The authors declare no conflicts of interest relevant to this study.

Availability Statement

PlanetWaves is freely available at https://github.com/Cornell-MIT/PlanetWaves and at https://doi.org/10.5281/zenodo.18906357. The University of Miami Wave Model is available at umwm.org. The Great Lakes buoy data was taken from NOAA's National Data Buoy Center (www.ndbc.noaa.gov). We acknowledge the use of the *Great Lakes Bathymetry: Lake Superior (3 arc-second grid)* data set, developed by the NOAA Great Lakes Environmental Research Lab, NOAA National Ocean Service, and the Canadian Hydrographic Service, and distributed by the NOAA National Centers for Environmental Information (NCEI), which can be accessed at: https://www.ncei.noaa.gov/access/metadata/landing-page/bin/iso?id=gov.noaa.ngdc.mgg.dem:greatlakes_bathymetry_lake_superior. The Unity 3D surface mesh generator algorithm and shaders in Figure 7 were adapted from https://github.com/gasgiant/FFT-Ocean under the MIT License. The Cassini SAR mosaics were assembled from images produced by the Cassini RADAR team (geomorph-sbirch.com/data-products/). Individual SAR data swaths that went into these mosaics are also freely available at the PDS Imaging Node(pds-imaging.jpl.nasa.gov/data/cassini/cassini_orbiter). The Jezero crater DTM mosaic can be found at https://astrogeology.usgs.gov/search/map/mars-

2020-jezero-crater-landing-site-products (Beyer et al., 2020; Fergason et al., 2020; Malin et al., 2007; Mangold et al., 2021).

Acknowledgments
This material is based upon work supported by the National Science Foundation Graduate Research Fellowship under Grant 214106 (U.G.S). C.E.D. was supported by the Future Investigators in NASA Earth and Space Sciences and Technology (FINESST) SMD's Graduate Student Research Fellowship under Grant 171064. M. C. was partly supported by the Office of Naval Research Grant N000142412598. This work was also supported by the NASA Cassini Data Analysis Program under Grants 80NSSC18K1057 and 80NSSC20K0484 (A. D. A., A. G. H., J. T. P.). The authors would like to thank Sara Seager for fascinating discussions about exoplanets and to Jason Barnes and Ralph Lorenz for constructive reviews that helped us improve the paper. The authors would also like to acknowledge Mark Donelan, who developed the original framework for this model but passed away before it could be completed.

References

Adams, K. D. (2023). Wind, waves, sediment transport, and potential for shoreline development on Earth and on Mars. *Icarus*, *405*, 115695. https://doi.org/10.1016/j.icarus.2023.115695

Alves, J. H. G. M., Banner, M. L., & Young, I. R. (2003). Revisiting the Pierson–Moskowitz asymptotic limits for fully developed wind waves. *Journal of Physical Oceanography*, *33*(7), 1301–1323. https://doi.org/10.1175/1520-0485(2003)033⟨1301:RTPALF⟩2.0.CO;2

Angelo, I., Rowe, J. F., Howell, S. B., Quintana, E. V., Still, M., Mann, A. W., et al. (2017). Kepler-1649b: An Exo-Venus in the solar neighborhood. *The Astronomical Journal*, *153*(4), 162. https://doi.org/10.3847/1538-3881/aa615f

Ashton, A. D., Murray, A. B., Littlewood, R., Lewis, D. A., & Hong, P. (2009). Fetch-limited self-organization of elongate water bodies. *Geology*, *37*(2), 187–190. https://doi.org/10.1130/G25299A.1

Banfield, D., Donelan, M. A., & Cavaleri, L. (2015). Winds, waves and shorelines from ancient Martian seas. *Icarus*, *250*, 368–383. https://doi.org/10.1016/j.icarus.2014.12.001

Barnes, J., Soderblom, J. M., Brown, R. H., Soderblom, L. A., Stephan, K., Jaumann, R., et al. (2011). Wave constraints for Titan's Jingpo Lacus and Kraken Mare from VIMS specular reflection light curves. *Icarus*, *211*(1), 722–731. https://doi.org/10.1016/j.icarus.2010.09.022

Barnes, J., Sotin, C., Soderblom, J., Brown, R., Hayes, A., Donelan, M. A., et al. (2014). Cassini/VIMS observes rough surfaces on Titan's Punga mare in specular reflection. https://doi.org/10.1186/s13535-014-0003-4

Benjamin, T. B. (1959). Shearing flow over a wavy boundary. *Journal of Fluid Mechanics*, *6*(2), 161–205. https://doi.org/10.1017/s0022112059000568

Beyer, R., Alexandrov, O., McMichael, S., Broxton, M., Lundy, M., & Husmann, K. (2020). *Neogeographytoolkit/stereopipeline 2.7. 0 (2.7. 0)*. Zenodo. https://doi.org/10.5281/zenodo.581187

Brown, R. H., Soderblom, L. A., Soderblom, J. M., Clark, R. N., Jaumann, R., Barnes, J. W., et al. (2008). The identification of liquid ethane in Titan's Ontario Lacus. *Nature*, *454*(7204), 607–610. https://doi.org/10.1038/nature07100

Cadieux, C., Doyon, R., MacDonald, R. J., Turbet, M., Lim, O., & Valencia, D. (2024). Transmission Spectroscopy of the habitable Zone Exoplanet LHS 1140 b with JWST/NIRISS. arXiv. (arXiv:2406.15136 [astro-ph])

Cadieux, C., Plotnykov, M., Doyon, R., Valencia, D., Jahandar, F., Dang, L., et al. (2024). New Mass and Radius Constraints on the LHS 1140 planets: LHS 1140 b is either a Temperate Mini-Neptune or a Water world. *The Astrophysical Journal Letters*, *960*(1), L3. https://doi.org/10.3847/2041-8213/ad1691

Charnay, B., Forget, F., Tobie, G., Sotin, C., & Wordsworth, R. D. (2014). Titan's past and future: 3D modeling of a pure nitrogen atmosphere and geological implications. *Icarus*, *241*, 269–279. https://doi.org/10.1016/j.icarus.2014.07.009

Chen, S. S., & Curcic, M. (2016). Ocean surface waves in hurricane Ike (2008) and superstorm sandy (2012): Coupled model predictions and observations. *Ocean Modelling*, *103*, 161–176. https://doi.org/10.1016/j.ocemod.2015.08.005

Cordier, D., Mousis, O., Lunine, J. I., Lavvas, P., & Vuitton, V. (2009). An estimate of the chemical composition of Titan's Lakes. *The Astrophysical Journal*, *707*(2), L128–L131. https://doi.org/10.1088/0004-637X/707/2/L128

Curcic, M. (2025). Revisiting the hydrodynamic modulation of short surface waves by longer waves. *Journal of Fluid Mechanics*, *1015*, A20. https://doi.org/10.1017/jfm.2025.10376

Curcic, M., & Haus, B. K. (2020). Revised estimates of Ocean surface drag in strong winds. *Geophysical Research Letters*, *47*(10), e2020GL087647. https://doi.org/10.1029/2020GL087647

De Toffoli, B., Plesa, A., Hauber, E., & Breuer, D. (2021). Delta deposits on Mars: A global perspective. *Geophysical Research Letters*, *48*(17), e2021GL094271. https://doi.org/10.1029/2021GL094271

Di Achille, G., & Hynek, B. M. (2010). Ancient ocean on Mars supported by global distribution of deltas and valleys. *Nature Geoscience*, *3*(7), 459–463. https://doi.org/10.1038/ngeo891

Dickson, J., Lamb, M., Williams, R., Hayden, A., & Fischer, W. (2021). The global distribution of depositional rivers on early Mars. *Geology*, *49*(5), 504–509. https://doi.org/10.1130/G48457.1

Donelan, M. A. (2001). A nonlinear dissipation function due to wave breaking. *Proc. ECMWF Workshop on Ocean Wave Forecasting*.

Donelan, M. A., Curcic, M., Chen, S. S., & Magnusson, A. K. (2012). Modeling waves and wind stress. *Journal of Geophysical Research*, *117*(C11). https://doi.org/10.1029/2011JC007787

Donelan, M. A., Hamilton, D. J., & Hui, W. (1985). Directional spectra of wind-generated ocean waves. *Philosophical Transactions of the Royal Society of London. Series A, Mathematical and Physical Sciences*, *315*(1534), 509–562. https://doi.org/10.1098/rsta.1985.0054

Donelan, M. A., Haus, B. K., Plant, W. J., & Troianowski, O. (2010). Modulation of short wind waves by long waves. *Journal of Geophysical Research*, *115*(C10), 2009JC005794. https://doi.org/10.1029/2009JC005794

Donelan, M. A., Haus, B. K., Reul, N., Plant, W. J., Stiassnie, M., Graber, H. C., et al. (2004). On the limiting aerodynamic roughness of the ocean in very strong winds. *Geophysical Research Letters*, *31*(18), 2004GL019460. https://doi.org/10.1029/2004GL019460

Donelan, M. A., & Pierson, W. (1987). Radar scattering and equilibrium ranges in wind-generated waves with application to scatterometry. *Journal of Geophysical Research*, *92*(C5), 4971–5029. https://doi.org/10.1029/JC092iC05p04971

Donelan, M. A., & Plant, W. J. (2009). A threshold for wind-wave growth. *Journal of Geophysical Research*, *114*(C7). https://doi.org/10.1029/2008JC005238

Ehlmann, B. L., Mustard, J. F., Murchie, S. L., Bibring, J.-P., Meunier, A., Fraeman, A. A., & Langevin, Y. (2011). Subsurface water and clay mineral formation during the early history of Mars. *Nature*, *479*(7371), 53–60. https://doi.org/10.1038/nature10582

Fergason, R., Hare, T., Mayer, D., Galuszka, D., Redding, B., Smith, E., et al. (2020). Mars 2020 terrain relative navigation flight product generation: Digital terrain model and orthorectified image mosaic. In *51st annual lunar and planetary science conference*. Retrieved from https://www.hou.usra.edu/meetings/lpsc2020/pdf/2020.pdf

Folkner, W. M., Asmar, S. W., Border, J. S., Franklin, G. W., Finley, S. G., Gorelik, J., et al. (2006). Winds on Titan from ground-based tracking of the Huygens probe. *Journal of Geophysical Research*, *111*(E7). https://doi.org/10.1029/2005JE002649

Ghafoor, N. A. L., Zarnecki, J. C., Challenor, P., & Srokosz, M. A. (2000). Wind-Driven surface waves on Titan. *Journal of Geophysical Research*, *105*(E5), 12077–12091. https://doi.org/10.1029/1999je001066

Grare, L., Peirson, W. L., Branger, H., Walker, J. W., Giovanangeli, J.-P., & Makin, V. (2013). Growth and dissipation of wind-forced, deep-water waves. *Journal of Fluid Mechanics*, *722*, 5–50. https://doi.org/10.1017/jfm.2013.88

21699100, 2026, 4, Downloaded from https://agupubs.onlinelibrary.wiley.com/doi/10.1029/2025JE009490 by Cochrane Russian Federation, Wiley Online Library on [30/04/2026]. See the Terms and Conditions (https://onlinelibrary.wiley.com/terms-and-conditions) on Wiley Online Library for rules of use; OA articles are governed by the applicable Creative Commons License

Grima, C., Mastrogiuseppe, M., Hayes, A. G., Wall, S. D., Lorenz, R. D., Hofgartner, J. D., et al. (2017). Surface roughness of Titan's hydrocarbon seas. *Earth and Planetary Science Letters*, *474*, 20–24. https://doi.org/10.1016/j.epsl.2017.06.007

Hasselman, K., Barnett, T. P., Bouws, E., Carlson, H., Cartwright, D. E., Enke, K., et al. (1973). *Measurements of wind-wave growth and swell decay during the Joint North Sea Wave Project (JONSWAP). Hasselmann, Klaus, et al. "Measurements of wind-wave growth and swell decay during the Joint North Sea Wave Project (JONSWAP)*. Ergaenzungsheft zur Deutschen Hydrographischen Zeitschrift, Reihe A.

Hayes, A. G. (2016). The Lakes and Seas of Titan. *Annual Review of Earth and Planetary Sciences*, *44*(1), 57–83. https://doi.org/10.1146/annurev-earth-060115-012247

Hayes, A. G., Lorenz, R., Donelan, M. A., Manga, M., Lunine, J., Schneider, T., et al. (2013). Wind driven capillary-gravity waves on Titan's lakes: Hard to detect or non-existent? *Icarus*, *225*(1), 403–412. https://doi.org/10.1016/j.icarus.2013.04.004

Heslar, M. F., & Barnes, J. W. (2025). Sea surface and hydrological activity observed in titan's punga mare. *The Planetary Science Journal*, *6*(3), 74. https://doi.org/10.3847/psj/adbc9e

Heslar, M. F., Barnes, J. W., Soderblom, J. M., Seignovert, B., Dhingra, R. D., & Sotin, C. (2020). Tidal currents detected in kraken mare straits from cassini vims sun glitter observations. *The Planetary Science Journal*, *1*(2), 35. https://doi.org/10.3847/psj/aba191

Hu, R., Bello-Arufe, A., Zhang, M., Paragas, K., Zilinskas, M., Van Buchem, C., et al. (2024). A secondary atmosphere on the rocky exoplanet 55 Cancri e. *Nature*, *630*(8017), 609–612. https://doi.org/10.1038/s41586-024-07432-x

Hu, R., & Thomas, T. B. (2022). A nitrogen-rich atmosphere on ancient Mars consistent with isotopic evolution models. *Nature Geoscience*, *15*(2), 106–111. https://doi.org/10.1038/s41561-021-00886-y

Huppert, K. L., Perron, J. T., & Ashton, A. D. (2020). The influence of wave power on bedrock sea-cliff erosion in the Hawaiian Islands. *Geology*, *48*(5), 499–503. https://doi.org/10.1130/G47113.1

Imboden, D. M., & Wüest, A. (1995). Mixing mechanisms in Lakes. In A. Lerman, D. M. Imboden, & J. R. Gat (Eds.), *Physics and chemistry of Lakes* (pp. 83–138). Springer Berlin Heidelberg. https://doi.org/10.1007/978-3-642-85132-2_4

Janssen, P. A. E. M. (1989). Wave-Induced stress and the drag of air flow over Sea waves. *Journal of Physical Oceanography*, *19*(6), 745–754. https://doi.org/10.1175/1520-0485(1989)019<0745:wisatd>2.0.co;2

Janssen, P. A. E. M., Doyle, J. D., Bidlot, J., Hansen, B., Isaksen, L., & Viterbro, P. (2002). Impact and feedback of ocean waves on the atmosphere. *Advances in Fluid Mechanics*, *33*, 155–198.

Jeffreys, H. (1925). On the formation of water waves by wind. *Proceedings of the Royal Society of London*, *107*(742), 189–206. https://doi.org/10.1098/rspa.1925.0015

Kahma, K. K., & Donelan, M. A. (1988). A laboratory study of the minimum wind speed for wind wave generation. *Journal of Fluid Mechanics*, *192*, 339–364. https://doi.org/10.1017/S0022112088001892

Khuller, A. R., & Clow, G. D. (2024). Turbulent fluxes and Evaporation/Sublimation rates on Earth, Mars, Titan, and exoplanets. *Journal of Geophysical Research: Planets*, *129*(4), e2023JE008114. https://doi.org/10.1029/2023JE008114

Kinsman, B. (1965). *Wind waves: Their generation and propagation on the Ocean surface*. Prentice-Hall, Inc.

Kitaigorodskii, S. A. (1983). On the theory of the equilibrium range in the spectrum of wind-generated gravity waves. *Journal of Physical Oceanography*, *13*(5), 816–827. https://doi.org/10.1175/1520-0485(1983)013⟨0816:OTTOTE⟩2.0.CO;2

Kite, E. S., Howard, A. D., Lucas, A. S., Armstrong, J. C., Aharonson, O., & Lamb, M. P. (2015). Stratigraphy of Aeolis Dorsa, Mars: Stratigraphic context of the great river deposits. *Icarus*, *253*, 223–242. https://doi.org/10.1016/j.icarus.2015.03.007

Kite, E. S., Williams, J.-P., Lucas, A., & Aharonson, O. (2014). Low palaeopressure of the Martian atmosphere estimated from the size distribution of ancient craters. *Nature Geoscience*, *7*(5), 335–339. https://doi.org/10.1038/ngeo2137

Komar, P. D. (1998). Wave erosion of a massive artificial coastal landslide. *Earth Surface Processes and Landforms*, *23*(5), 415–428. https://doi.org/10.1002/(SICI)1096-9837(199805)23:5⟨415::AID-ESP855⟩3.0.CO;2-T

Komen, G., Cavaleri, L., Donelan, M. A., Hasselmann, K., Hasselmann, S., & Janssen, P. (1994). The physical description of wave evolution. In *Dynamics and modelling of Ocean waves* (pp. 69–202). Cambridge University Press.

Kraal, E. R., Asphaug, E., Moore, J. M., & Lorenz, R. D. (2006). Quantitative geomorphic modeling of Martian bedrock shorelines. *Journal of Geophysical Research*, *111*(E3). https://doi.org/10.1029/2005JE002567

Kurokawa, H., Kurosawa, K., & Usui, T. (2018). A lower limit of atmospheric pressure on early Mars inferred from nitrogen and argon isotopic compositions. *Icarus*, *299*, 443–459. https://doi.org/10.1016/j.icarus.2017.08.020

Large, W. G., & Pond, S. (1981). Open Ocean momentum flux measurements in moderate to strong winds. *Journal of Physical Oceanography*, *11*(3), 324–336. https://doi.org/10.1175/1520-0485(1981)011<0324:oomfmi>2.0.co;2

Le Gall, A., Malaska, M. J., Lorenz, R. D., Janssen, M. A., Tokano, T., Hayes, A. G., et al. (2016). Composition, seasonal change, and bathymetry of Ligeia Mare, Titan, derived from its microwave thermal emission: Microwave Radiometry of Ligeia Mare. *Journal of Geophysical Research: Planets*, *121*(2), 233–251. https://doi.org/10.1002/2015JE004920

Liu, P. C. (1989). On the slope of the equilibrium range in the frequency spectrum of wind waves. *Journal of Geophysical Research*, *94*(C4), 5017–5023. https://doi.org/10.1029/JC094iC04p05017

Lora, J. M., Battalio, J. M., Yap, M., & Baciocco, C. (2022). Topographic and orbital forcing of titan's hydroclimate. *Icarus*, *384*, 115095. https://doi.org/10.1016/j.icarus.2022.115095

Lorenz, R. D., & Hayes, A. G. (2012). The growth of wind-waves in Titan's hydrocarbon seas. *Icarus*, *219*(1), 468–475. https://doi.org/10.1016/j.icarus.2012.03.002

Lorenz, R. D., Kraal, E. R., Eddlemon, E. E., Cheney, J., & Greeley, R. (2005). Sea-surface wave growth under extraterrestrial atmospheres: Preliminary wind tunnel experiments with application to Mars and Titan. *Icarus*, *175*(2), 556–560. https://doi.org/10.1016/j.icarus.2004.11.019

Lorenz, R. D., McKay, C. P., & Lunine, J. I. (1997). Photochemically driven collapse of Titan's atmosphere. *Science*, *275*(5300), 642–644. https://doi.org/10.1126/science.275.5300.642

Lorenz, R. D., Newman, C., & Lunine, J. I. (2010). Threshold of wave generation on Titan's lakes and seas: Effect of viscosity and implications for Cassini observations. *Icarus*, *207*(2), 932–937. https://doi.org/10.1016/j.icarus.2009.12.004

Malaska, M. J., & Hodyss, R. (2014). Dissolution of benzene, naphthalene, and biphenyl in a simulated Titan lake. *Icarus*, *242*, 74–81. https://doi.org/10.1016/j.icarus.2014.07.022

Malin, M. C., Bell, J. F., III, Cantor, B. A., Caplinger, M. A., Calvin, W. M., Clancy, R. T., et al. (2007). Context camera investigation on board the mars reconnaissance orbiter. *Journal of Geophysical Research*, *112*(E5). https://doi.org/10.1029/2006JE002808

Mangold, N., Caravaca, G., Gupta, S., Williams, R. M. E., Dromart, G., Gasnault, O., et al. (2024). Architecture of fluvial and deltaic deposits exposed along the Eastern edge of the Western fan of jezero crater, Mars. *Journal of Geophysical Research: Planets*, *129*(3), e2023JE008204. https://doi.org/10.1029/2023JE008204

Mangold, N., Gupta, S., Gasnault, O., Dromart, G., Tarnas, J. D., Sholes, S. F., et al. (2021). Perserverance rover reveals an Ancient Delta-Lake system and flood deposits at jezero crater, Mars. *Science*, *374*(6568), 711–717. https://doi.org/10.1126/science.abl4051

21699100, 2026, 4, Downloaded from https://agupubs.onlinelibrary.wiley.com/doi/10.1029/2025JE009490 by Cochrane Russian Federation, Wiley Online Library on [30/04/2026]. See the Terms and Conditions (https://onlinelibrary.wiley.com/terms-and-conditions) on Wiley Online Library for rules of use; OA articles are governed by the applicable Creative Commons License

Mastrogiuseppe, M., Hayes, A., Poggiali, V., Lunine, J., Lorenz, R., Seu, R., et al. (2018). Bathymetry and composition of Titan's Ontario Lacus derived from Monte Carlo-based waveform inversion of Cassini RADAR altimetry data. *Icarus*, *300*, 203–209. https://doi.org/10.1016/j.icarus.2017.09.009

Mastrogiuseppe, M., Poggiali, V., Hayes, A. G., Lunine, J. I., Seu, R., Mitri, G., & Lorenz, R. D. (2019). Deep and methane-rich lakes on Titan. *Nature Astronomy*, *3*(6), 535–542. https://doi.org/10.1038/s41550-019-0714-2

Miles, J. W. (1957). On the generation of surface waves by shear flows. *Journal of Fluid Mechanics*, *3*(2), 185–204. https://doi.org/10.1017/s0022112057000567

Mischna, M. A., Kasting, J. F., Pavlov, A., & Freedman, R. (2000). Influence of carbon dioxide clouds on early martian climate. *Icarus*, *145*(2), 546–554. https://doi.org/10.1006/icar.2000.6380

Mitchell, J. L., & Lora, J. M. (2016). The climate of Titan. *Annual Review of Earth and Planetary Sciences*, *44*(1), 353–380. https://doi.org/10.1146/annurev-earth-060115-012428

Mondro, C. A., Fedo, C. M., Grotzinger, J. P., Lamb, M. P., Gupta, S., Dietrich, W. E., et al. (2025). Wave ripples formed in ancient, ice-free lakes in Gale crater, Mars. *Science Advances*, *11*(3), eadr0010. https://doi.org/10.1126/sciadv.adr0010

Monin, A. S., & Obukhov, A. M. (1954). *Basic laws of turbulent mixing in the surface layer of the atmosphere* (Vol. 24). Trudy Geofizicheskogo Instituta AN SSSR.

Murase, T., & McBirney, A. R. (1973). Properties of some common igneous rocks and their melts at high temperatures. *Geological Society of America Bulletin*, *84*(11), 3563. https://doi.org/10.1130/0016-7606(1973)84⟨3563:POSCIR⟩2.0.CO;2

Nienhuis, J. H., Ashton, A. D., & Giosan, L. (2015). What makes a delta wave-dominated? *Geology*, *43*(6), 511–514. https://doi.org/10.1130/G36518.1

Nixon, C. A. (2024). The composition and chemistry of Titan's atmosphere. *ACS Earth and Space Chemistry*, *8*(3), 406–456. (arXiv:2402.17116 [astro-ph]). https://doi.org/10.1021/acsearthspacechem.2c00041

Olim, E., Lora, J. M., & Battalio, J. M. (2025). Methane storm characteristics and evolution in simulations of Titan's hydroclimate. *Icarus*, *425*, 116290. https://doi.org/10.1016/j.icarus.2024.116290

Palermo, R. V., Ashton, A. D., Soderblom, J. M., Birch, S. P. D., Hayes, A. G., & Perron, J. T. (2024). Signatures of wave erosion in Titan's coasts. *Science Advances*, *10*(25), eadn4192. https://doi.org/10.1126/sciadv.adn4192

Phillips, O. M. (1958). The equilibrium range in the spectrum of wind-generated waves. *Journal of Fluid Mechanics*, *4*(4), 426–434. https://doi.org/10.1017/S0022112058000550

Pierson, W. J., & Moskowitz, L. (1964). A proposed spectral form for fully developed wind seas based on the similarity theory of sa kitaigorodskii. *Journal of Geophysical Research*, *69*(24), 5181–5190. https://doi.org/10.1029/jz069i024p05181

Poggiali, V., Brighi, G., Hayes, A. G., Nicholson, P. D., MacKenzie, S., Lalich, D. E., et al. (2024). Surface properties of the seas of Titan as revealed by Cassini mission bistatic radar experiments. *Nature Communications*, *15*(1), 5454. https://doi.org/10.1038/s41467-024-49837-2

Poggiali, V., Hayes, A. G., Mastrogiuseppe, M., Le Gall, A., Lalich, D., Gómez-Leal, I., & Lunine, J. I. (2020). The bathymetry of Moray sinus at Titan's kraken mare. *Journal of Geophysical Research: Planets*, *125*(12), e2020JE006558. https://doi.org/10.1029/2020JE006558

Romero, L. (2019). Distribution of surface wave breaking fronts. *Geophysical Research Letters*, *46*(17–18), 10463–10474. https://doi.org/10.1029/2019gl083408

Rubin, D. M., Lapôtre, M. A. G., Stevens, A. W., Lamb, M. P., Fedo, C. M., Grotzinger, J. P., et al. (2022). Ancient winds, waves, and atmosphere in gale crater, Mars, inferred from sedimentary structures and wave modeling. *Journal of Geophysical Research: Planets*, *127*(4), e2021JE007162. https://doi.org/10.1029/2021JE007162

Schlichting, H., & Kestin, J. (1961). *Boundary layer theory* (9th ed., Vol. 121). Springer.

Schon, S. C., Head, J. W., & Fassett, C. I. (2012). An overfilled lacustrine system and progradational delta in Jezero crater, Mars: Implications for Noachian climate. *Planetary and Space Science*, *67*(1), 28–45. https://doi.org/10.1016/j.pss.2012.02.003

Seager, S. (2013). Exoplanet habitability. *Science*, *340*(6132), 577–581. https://doi.org/10.1126/science.1232226

Seager, S., & Dotson, R. (2010). *Exoplanets*. The University of Arizona Press.

Steckloff, J. K., Soderblom, J. M., Farnsworth, K. K., Chevrier, V. F., Hanley, J., Soto, A., et al. (2020). Stratification dynamics of Titan's Lakes via methane evaporation. *The Planetary Science Journal*, *1*(2), 26. https://doi.org/10.3847/PSJ/ab974e

Stofan, E. R., Elachi, C., Lunine, J. I., Lorenz, R. D., Stiles, B., Mitchell, K. L., et al. (2007). The lakes of Titan. *Nature*, *445*(7123), 61–64. https://doi.org/10.1038/nature05438

Tan, P., Smith, A. W., Curcic, M., & Haus, B. K. (2023). Laboratory wave and stress measurements quantify the aerodynamic sheltering in extreme winds. *Journal of Geophysical Research: Oceans*, *128*(4), e2022JC019505. https://doi.org/10.1029/2022jc019505

Thomson, G. H. (1996). The DIPPR databases. *International Journal of Thermophysics*, *17*(1), 223–232. https://doi.org/10.1007/BF01448224

Viúdez-Moreiras, D., De La Torre, M., Gómez-Elvira, J., Lorenz, R. D., Apéstigue, V., Guzewich, S., et al. (2022). Winds at the Mars 2020 landing site. 2. Wind variability and turbulence. *Journal of Geophysical Research: Planets*, *127*(12), e2022JE007523. https://doi.org/10.1029/2022JE007523

Viúdez-Moreiras, D., Lemmon, M., Newman, C. E., Guzewich, S., Mischna, M., Gómez-Elvira, J., et al. (2022). Winds at the Mars 2020 landing site: 1. Near-Surface wind patterns at jezero crater. *Journal of Geophysical Research: Planets*, *127*(12), e2022JE007522. https://doi.org/10.1029/2022JE007522

Wall, S., Hayes, A., Bristow, C., Lorenz, R., Stofan, E., Lunine, J., et al. (2010). Active shoreline of Ontario Lacus, Titan: A morphological study of the lake and its surroundings. *Geophysical Research Letters*, *37*(5). https://doi.org/10.1029/2009GL041821

Wordsworth, R. D. (2016). The climate of early Mars. *Annual Review of Earth and Planetary Sciences*, *44*(1), 381–408. https://doi.org/10.1146/annurev-earth-060115-012355

Wordsworth, R. D., & Kreidberg, L. (2022). Atmospheres of rocky exoplanets. *Annual Review of Astronomy and Astrophysics*, *60*(1), 159–201. https://doi.org/10.1146/annurev-astro-052920-125632

Wye, L. C., Zebker, H. A., & Lorenz, R. D. (2009). Smoothness of Titan's Ontario Lacus: Constraints from Cassini RADAR specular reflection data. *Geophysical Research Letters*, *36*(16). https://doi.org/10.1029/2009GL039588

Young, I. (1995). The determination of confidence limits associated with estimates of the spectral peak frequency. *Ocean Engineering*, *22*(7), 669–686. https://doi.org/10.1016/0029-8018(95)00002-3

Young, I. (2020). Wind-Generated waves. In *Ocean wave dynamics*. World Scientific.

Zebker, H., Hayes, A., Janssen, M., Le Gall, A., Lorenz, R., & Wye, L. (2014). Surface of Ligeia Mare, Titan, from Cassini altimeter and radiometer analysis. *Geophysical Research Letters*, *41*(2), 308–313. https://doi.org/10.1002/2013GL058877

Zugger, M. E., Kasting, J. F., Williams, D. M., Kane, T. J., & Philbrick, C. R. (2010). Light scattering from exoplanet Oceans and atmospheres. *The Astrophysical Journal*, *723*(2), 1168–1179. https://doi.org/10.1088/0004-637X/723/2/1168

21699100, 2026, 4, Downloaded from https://agupubs.onlinelibrary.wiley.com/doi/10.1029/2025JE009490 by Cochrane Russian Federation, Wiley Online Library on [30/04/2026]. See the Terms and Conditions (https://onlinelibrary.wiley.com/terms-and-conditions) on Wiley Online Library for rules of use; OA articles are governed by the applicable Creative Commons License